The Astronomical Journal, 159:168 (19pp), 2020 April https://doi.org/10.3847/1538-3881/ab789a

Probing UV-sensitive Pathways for CN and HCN Formation in Protoplanetary Disks with the *Hubble Space Telescope*

Nicole Arulanantham[1], Kevin France[1], Paolo Cazzoletti[2], Anna Miotello[3], Carlo F. Manara[3], P. Christian Schneider[4], Keri Hoadley[5], Ewine F. van Dishoeck[2,6], and Hans Moritz Günther[7]

[1] Laboratory for Atmospheric and Space Physics, University of Colorado, 392 UCB, Boulder, CO 80303, USA
[2] Max-Planck-Institute for Extraterrestrial Physics (MPE), Giessenbachstr. 1, D-85748, Garching, Germany
[3] European Southern Observatory, Karl-Schwarzschild-Str. 2, D-85748 Garching bei München, Germany
[4] Hamburger Sternwarte, Gojenbergsweg 112, D-21029 Hamburg, Germany
[5] Department of Astronomy, California Institute of Technology, 1200 East California Blvd., Pasadena, CA 91125, USA
[6] Leiden Observatory, Leiden University, PO Box 9513, 2300 RA Leiden, The Netherlands
[7] MIT, Kavli Institute for Astrophysics and Space Research, 77 Massachusetts Ave., Cambridge, MA 02139, USA

Received 2019 November 15; revised 2020 February 17; accepted 2020 February 19; published 2020 March 23

Abstract

The UV radiation field is a critical regulator of gas-phase chemistry in surface layers of disks around young stars. In an effort to understand the relationship between photocatalyzing UV radiation fields and gas emission observed at infrared and submillimeter wavelengths, we present an analysis of new and archival *Hubble Space Telescope* (*HST*), *Spitzer*, ALMA, IRAM, and SMA data for five targets in the Lupus cloud complex and 14 systems in Taurus-Auriga. The *HST* spectra were used to measure Lyα and far-UV (FUV) continuum fluxes reaching the disk surface, which are responsible for dissociating relevant molecular species (e.g., HCN, N_2). Semi-forbidden C II] λ2325 and UV-fluorescent H_2 emission were also measured to constrain inner disk populations of C^+ and vibrationally excited H_2. We find a significant positive correlation between 14 μm HCN emission and fluxes from the FUV continuum and C II] λ2325, consistent with model predictions requiring N_2 photodissociation and carbon ionization to trigger the main CN/HCN formation pathways. We also report significant negative correlations between submillimeter CN emission and both C II] and FUV continuum fluxes, implying that CN is also more readily dissociated in disks with stronger FUV irradiation. No clear relationships are detected between either CN or HCN and Lyα or UV-H_2 emission. This is attributed to the spatial stratification of the various molecular species, which span several vertical layers and radii across the inner and outer disk. We expect that future observations with the *James Webb Space Telescope* will build on this work by enabling more sensitive IR surveys than were possible with *Spitzer*.

Unified Astronomy Thesaurus concepts: Protoplanetary disks (1300); Ultraviolet astronomy (1736); Young stellar objects (1834); Molecular spectroscopy (2095); Astrochemistry (75)

1. Introduction

Multiwavelength observations of gas- and dust-rich disks around young stars have allowed us to develop rudimentary maps of the composition and structure of planet-forming material. Infrared surveys with *Spitzer* (Öberg et al. 2008; Bottinelli et al. 2010; Pontoppidan et al. 2010; Salyk et al. 2011b; Pascucci et al. 2013) and *Herschel* (Dent et al. 2013) provided important constraints on warm molecular gas in surface layers of the inner disks ($r < 10$ au), contributing column densities and temperatures of critical molecular gas species (e.g., H_2O, CO_2). Submillimeter observations of star-forming regions with ALMA have revealed the structure of cold gas in the outer disks with unprecedented sensitivity and angular resolution (Ansdell et al. 2016, 2017; Barenfeld et al. 2016; Pascucci et al. 2016; Miotello et al. 2017; Tazzari et al. 2017; Long et al. 2018, 2019; Cazzoletti et al. 2019; van Terwisga et al. 2019; Williams et al. 2019), showing statistically significant trends in mass and radial extent as a function of cluster age and initial conditions of the parent cloud (e.g., angular momentum, temperature; Cazzoletti et al. 2019). Both observational and theoretical work demonstrate that the chemical evolution of molecular gas is strongly dependent on the ultraviolet radiation field reaching the surface of the disk (Aikawa et al. 2002; Chapillon et al. 2012; Walsh et al. 2012, 2015; Agúndez et al. 2018; Cazzoletti et al. 2018; Cleeves et al. 2018; Bergner et al. 2019; Miotello et al. 2019). However, the effects of disk geometry and varying UV flux are degenerate in physical–chemical models of the gas distributions (e.g., Cazzoletti et al. 2018), making it difficult to trace the precise locations of critical species within the disk in the absence of high angular resolution data sets.

Observational constraints on the UV flux reaching the disk surface are available from *Hubble Space Telescope* (*HST*) surveys of young stars with circumstellar disks (e.g., France et al. 2012, 2014; Yang et al. 2012). The wavelength range available with the Cosmic Origins Spectrograph (*HST*-COS) includes Lyα emission ($\lambda = 1215.67$ Å) and a portion of the far-UV (FUV) continuum ($\lambda > 1090$ Å), providing estimates of key photochemical ingredients in the molecular gas disk (Bergin et al. 2003; Li et al. 2013). In addition to these direct tracers of the UV radiation field, emission lines from electronic transitions of H_2 are also detected in *HST*-COS and *HST*-STIS spectra (Herczeg et al. 2002; France et al. 2012). These features originate in surface layers close to the star (Hoadley et al. 2015), providing an independent way to estimate the UV flux reaching the innermost regions of the disk (Herczeg et al. 2004; Schindhelm et al. 2012b).

In this work, we present new and archival *HST*-COS and *HST*-STIS observations of a sample of five young systems in the ~3 Myr Lupus complex. We interpret our measurements of

Table 1
Stellar and Disk Properties

Target	Distance (pc)	M_* ($M_\odot$)	A_V (mag)	i (°)	$r_{cav,dust}$ (au)	$r_{cav,gas}$ (au)	References
RU Lupi[a]	159	0.8	0.07	~18°5	14, 17, 21, 24, 29.1, 34, 42, 50	...	(a), (b), (c)
RY Lupi	158	1.47	0.1	68	50	50	(a), (d)
MY Lupi[a]	156	1.02	0.04	73	8, 20, 30, 40	25	(a), (b), (d)
Sz 68	154	2.13	0.15	34	...	...	(a), (e)
J1608-3070	155	1.81	0.055	74	75	60	(a), (d)

Notes.
[a] High-resolution ALMA images of RU Lupi have revealed a series of rings inside ~50 au (Huang et al. 2018). The two rings with constrained values have inclinations of 20° and 17°, so we use an average of the two. For both RU Lupi and MY Lupi, the $r_{cav,dust}$ radii are locations of the dust rings resolved by Huang et al. (2018).
References. (a) Bailer-Jones et al. (2018); (b) Huang et al. (2018); (c) van der Marel et al. (2018); (d) Ansdell et al. (2016).

the UV radiation field and molecular gas features in the context of submillimeter CN observations and infrared HCN emission from *Spitzer*, including disks in Taurus-Auriga for comparison. We focus on these two molecules because of the strong dependence of their physical distributions on the UV radiation field (Agúndez et al. 2008, 2018; Cazzoletti et al. 2018; Bergner et al. 2019; Greenwood et al. 2019). Our data set therefore allows us to observationally examine the theoretical relationships between molecular gas emission and UV radiation fields, in turn constraining physical–chemical models that map abundances of volatile elements (C, N, and H). This information may be particularly useful in disk regions where gas-phase oxygen is depleted and emission from more abundant species (e.g., CO) is fainter than expected (Miotello et al. 2017; Schwarz et al. 2018). The radial distributions of these molecules can then inform us about the composition of material available for *in situ* protoplanetary accretion, setting important initial conditions for atmospheric chemistry (see, e.g., Madhusudhan et al. 2011). To this end, we discuss the relationships between spectral tracers of the UV radiation field and integrated fluxes from CN and HCN, with particular consideration given to the impact of disk geometry and the optical depth of the molecular gas.

2. Targets and Observations

2.1. A Sample of Young Disks in the Lupus Complex

Our sample consists of five young stars with circumstellar disks in the nearby ($d \sim 160$ pc; Bailer-Jones et al. 2018) Lupus cloud complex: RY Lupi, RU Lupi, MY Lupi, Sz 68, and J1608-3070. Table 1 lists the properties of each target from Alcalá et al. (2017), including stellar mass, disk inclination, and visual extinction (A_V). Interstellar A_V is low along the line of sight to the Lupus clouds (Alcalá et al. 2017), making the region well-suited for UV observations. This group of young systems shows a broad range of outer disk morphologies in ALMA observations of their gas and dust distributions. At the time of the new *HST* observations, two targets (Sz 68, RU Lupi) were categorized as full, primordial disks and three (MY Lupi, RY Lupi, J1608-3070) were identified as transition disks from submillimeter images ($r_{cav} = 25$, 50, 75 au; van der Marel et al. 2018) under the traditional classification scheme (see, e.g., Strom et al. 1989; Skrutskie et al. 1990). However, RY Lupi differs from MY Lupi and J1608-3070 in that it has strong 10 μm silicate emission (Kessler-Silacci et al. 2006) from warm grains close to the central star and undergoes periodic optical variability attributed to occultations by a warped inner disk (Manset et al. 2009). These signatures are not typical of depleted transition disks, indicating that the clearing of material seen inside 50 au is a gap, rather than a cavity (Arulanantham et al. 2018; van der Marel et al. 2018). RU Lupi and MY Lupi were observed at high resolution (~5 au) with ALMA as part of the Disk Substructures at High Angular Resolution Project (DSHARP; Andrews et al. 2018), which revealed multiple rings of 1.25 mm continuum emission within each disk (Huang et al. 2018). Sz 68, a triple system that was also included in DSHARP (Andrews et al. 2018), consists of a close binary and a distant third companion. The *HST* and ALMA observations presented here include emission from both binary components. However, the secondary star (component B) and its disk are much smaller and fainter than the circumprimary disk: $F_{star\,B}/F_{star\,A} = 0.17$ (Ghez et al. 1997) and $I_{peak,diskB}/I_{peak,diskA} = 0.23$ (Kurtovic et al. 2018), indicating that the bulk of the UV emission comes from the primary component.

These systems were selected for follow-up with *HST* after a large ALMA survey of the Lupus clouds identified them as hosts to some of the most massive dust disks in the region (Ansdell et al. 2016, 2018). However, physical–chemical models of the ^{13}CO and C^{18}O emission demonstrate that the total gas masses are unexpectedly low (Miotello et al. 2016, 2017), which can be attributed to either shorter timescales than predicted for removing gas from the disk (e.g., via external photoevaporation) or chemical pathways that trap carbon in larger molecules with higher freeze-out temperatures. Because UV photons are critical regulators of chemical processes in disk environments (see e.g., Aikawa et al. 2002; Bergin et al. 2003; Bethell & Bergin 2011; Walsh et al. 2012, 2015; Cazzoletti et al. 2018; Visser et al. 2018), the *HST* data we present here provide currently missing observational constraints on the levels of irradiation at the surface of the gas disk.

2.2. Observations

All five systems were observed with the *HST*, using both the Cosmic Origins Spectrograph (COS; Green et al. 2012) and the Space Telescope Imaging Spectrograph (STIS; Woodgate et al. 1997a, 1997b). Table 2 lists exposure times and program IDs for the observations. The FUV spectra for three of our targets were previously presented in France et al. (2012) (RU Lupi), Arulanantham et al. (2018) (RY Lupi), and Alcala et al. (2019) (MY Lupi).

Five different modes of *HST*-COS and *HST*-STIS were used to observe four of our systems, to cover wavelengths from

Table 2
Observations of Young Systems in Lupus

	RU Lupi[a]	RY Lupi	MY Lupi	Sz 68	J1608-3070
Program ID	12036, 8157	14469	14604	14604	14604
			Exposure Time (s) Observation Date		
HST-COS G140L	⋯	2448	5658	5538	5574
(λ1280; $R \sim 1500$)	⋯	2016 Jun 16	2018 Sep 8	2018 Jul 27	2018 Jul 30
HST-COS G130M	1686	654	1242	1212	1218
(λ1291; $R \sim 16000$)	2012 Jul 20	2016 Jun 16	2018 Sep 8	2018 Jul 27	2018 Jul 30
HST-COS G160M	1938	648	1296	1266	1278
(λ1577; $R \sim 16000$)	2012 Jul 21	2016 Jun 16	2018 Sep 8	2018 Jul 27	2018 Jul 30
HST-STIS G230L	⋯	2400	2028	1968	1986
(λ2375; $R \sim 1000$)	⋯	2016 Jun 16	2018 Sep 8	2018 Jul 26	2018 Jul 30
HST-STIS G430L	120	60	60	60	60
(λ4300; $R \sim 1000$)	2001 Jul 12	2016 Jun 16	2018 Sep 8	2018 Jul 26	2018 Jul 30

Note.
[a] The G160M λ1589 setting was used for RU Lupi instead of λ1577.

1100 to 5000 Å. NUV coverage is not included for the fifth star, RU Lupi, which was observed as part of a different program. These data were used to extrapolate the FUV continuum down to the hydrogen ionization edge at 912 Å, which is a critical region for photodissociation of abundant molecular species (e.g., H_2 and CO) and gas-phase chemistry but not readily accessible with available UV facilities (France et al. 2014). All five spectral modes were then stitched together to produce a SED for each system using the methods outlined in France et al. (2014) and Arulanantham et al. (2018). Figure 1 shows an overview of the SEDs, highlighting the strong contribution from the accretion-dominated NUV continuum ($\lambda \sim 3000$–4000 Å). Accretion processes enhance the FUV continuum as well, but the total flux at $\lambda < 2000$ Å is dominated by line emission from hot, atomic gas (e.g., Lyα, C IV, C II). Our resulting library of radiation fields, which encompasses far-ultraviolet to optical wavelengths, is available to the community.[8] We anticipate that the data will be used in gas-phase chemical modeling efforts that require an understanding of stellar irradiation at the disk surface.

Submillimeter CN fluxes for this work were taken from the literature, providing measurements of gas in the cold, outer regions of the disk. The data were acquired with the SMA (Öberg et al. 2010, 2011), the IRAM 30 m telescope (Guilloteau et al. 2013), and ALMA (van Terwisga et al. 2019), causing the full sample to span several different observing configurations and spectral features. While the Lupus ALMA survey measured fluxes from the strongest $N = 3 - 2$, $J = 7/2 - 5/2$ hyperfine CN transitions (van Terwisga et al. 2019), $N = 2 - 1, J = 5/2 - 3/2$ features are reported from targets in Taurus-Auriga (Öberg et al. 2011; Guilloteau et al. 2013). To convert the fluxes from different data sets to comparable quantities, we adopted the methodology of van Terwisga et al. (2019) and used the ratio

$$\frac{N = 2 - 1, J = 5/2 - 3/2}{N = 3 - 2, J = 7/2 - 5/2} = 1.6 \quad (1)$$

to obtain CN $N = 2 - 1, J = 5/2 - 3/2$ flux estimates for the Lupus disks. This scaling accounts for the gas temperature distribution within the disk, under the assumption that the CN emission is optically thin. The value chosen by van Terwisga et al. (2019), which we use here, is the median from the grid of models studied by Cazzoletti et al. (2018), which spanned a range from 1.1 to 2.1.

The total $N = 2 - 1$, $J = 5/2 - 3/2$ flux in all 19 hyperfine transitions listed by Guilloteau et al. (2013) was estimated by scaling the flux in the three strongest features (226.874, 226.887, and 226.892 GHz) by a factor of 1.67, as calculated by those authors from the measured flux ratios. We applied the same scaling to the 226.874 GHz fluxes from Öberg et al. (2010, 2011). However, these measurements likely are slightly underestimated because they do not include the weaker emission lines at 226.887 and 226.892 GHz. We depict them as lower limits in the figures presented here. We also note that different methods were used to derive the CN fluxes, with van Terwisga et al. (2019) using aperture photometry and Guilloteau et al. (2013) and Öberg et al. (2010, 2011) using the integrated spectral lines. Guilloteau et al. (2013) account for beam dilution in their flux measurements by incorporating a "beam filling factor" in their CN line fitting procedure, while Öberg et al. (2010, 2011) estimate synthesized beam sizes. We emphasize that the differences in observing methodologies outlined here introduce systematic uncertainties into our analysis that may contribute ~30% to the Lupus CN fluxes and ~50% to the Öberg et al. (2010, 2011) measurements that are scaled and presented here.

Infrared HCN features, originating in the warmer inner disk, were measured directly from observations with the InfraRed Spectrograph (IRS) onboard the *Spitzer Space Telescope* (Houck et al. 2004). All targets except J1608-3070 were observed in the high-resolution mode ($R \sim 600$) over the course of several different observing programs. The data were retrieved from the Combined Atlas of Sources with *Spitzer* IRS Spectra (CASSIS; Lebouteiller et al. 2011, 2015), which provides a complete catalog of *Spitzer*/IRS observations. Fluxes from the 14 μm HCN v_2 band were measured over the wavelength range defined for the feature in Najita et al. (2013). That work used slab

[8] http://cos.colorado.edu/~kevinf/ctts_fuvfield.html

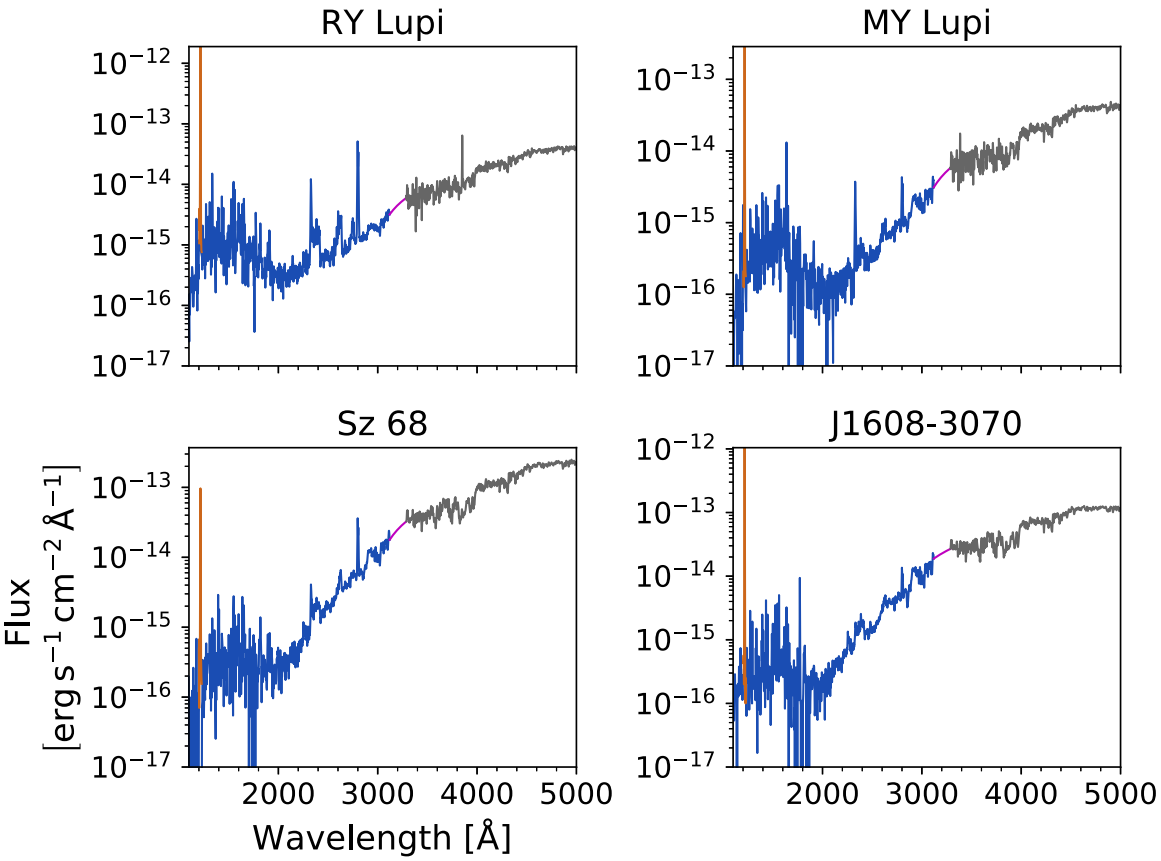

Figure 1. Panchromatic spectrum produced for four disks in Lupus by stitching together new data from five different observing modes of *HST*-COS (blue) and *HST*-STIS (gray). We include reconstructed model Lyα profiles (orange; see, e.g., Schindhelm et al. 2012b) in place of the observed features, which are contaminated by interstellar absorption and geocoronal emission. Interpolated fluxes spanning the overlap between gratings are shown in magenta. The spectra from RU Lupi and the disks in Taurus-Auriga were previously presented in Herczeg et al. (2005) and France et al. (2014).

Table 3
Spitzer/IRS PIDs and Fluxes and Submillimeter CN References

Target	Program ID	PI	Observation Date (yyyy mm dd)	HCN Fluxes (10^{-14} erg s^{-1} cm^{-2})	CN References
AA Tau	20363	J. Carr	2005 Oct 15	4.9 ± 0.7	Guilloteau et al. (2013)
BP Tau	20363	J. Carr	2006 Mar 19	6 ± 1	Guilloteau et al. (2013)
DE Tau	50641	J. Carr	2008 Oct 8	3 ± 1	Guilloteau et al. (2013)
DM Tau	30300	J. Najita	2007 Mar 24	2 ± 1	Guilloteau et al. (2013)
DR Tau	50641	J. Carr	2008 Oct 8	18 ± 3	Guilloteau et al. (2013)
DS Tau	50498	J. Houck	2008 Nov 9	9 ± 2	Guilloteau et al. (2013)
GM Aur	30300	J. Najita	2007 Mar 14	2 ± 1.5	Öberg et al. (2010)
HN Tau A	50641	J. Carr	2008 Oct 1	2.4 ± 0.4	…
LkCa 15	40338	J. Najita	2008 Nov 5	2.8 ± 0.6	Öberg et al. (2010)
MY Lupi	20611	C. Wright	2005 Aug 8	1.4 ± 0.2	van Terwisga et al. (2019)
RU Lupi	172	N. Evans	2004 Aug 30	12 ± 3	van Terwisga et al. (2019)
RY Lupi	172	N. Evans	2004 Aug 30	3 ± 2	van Terwisga et al. (2019)
SU Aur	50641	J. Carr	2008 Nov 5	8 ± 3	Guilloteau et al. (2013)
Sz 68	172	N. Evans	2004 Aug 30	8 ± 4	van Terwisga et al. (2019)
T Tau	40113	F. Lahuis	2008 Oct 1	130 ± 80	Guilloteau et al. (2013)
J1608-3070	…	…	…	…	van Terwisga et al. (2019)
V4046 Sgr	3580	M. Honda	2005 Apr 19	4.2 ± 0.7	Öberg et al. (2011)

models of the molecular gas disk to identify line-free spectral windows for each target, which we used as a reference for continuum subtraction. Although the measurement errors from the *Spitzer* spectra are ∼5%, the continuum subtraction procedure is likely the largest source of uncertainty in the final HCN fluxes. We quantify this by measuring the fluxes using three different sets of continuum regions defined by Pascucci et al. (2009), Teske et al. (2011), and Najita et al. (2013), finding that the resulting fluxes are consistent to within ∼20%. The average and standard deviation of the three measurements for each target are reported in Table 3, along with observing program IDs and PIs.

2.3. Archival HST Data from YSOs in Taurus-Auriga

To increase the sample size of this study and compare properties between different star-forming regions, we include all Taurus-Auriga sources from the literature with both submillimeter CN fluxes and UV spectra from *HST*-STIS and/or *HST*-COS. Disks in Taurus are roughly equivalent in age to the Lupus systems (~1–3 Myr; Andrews et al. 2013; Alcalá et al. 2014) and have similar dust mass distributions (Ansdell et al. 2016; Pascucci et al. 2016), making it easier to isolate the impact of the UV radiation field on the molecular gas distributions. The UV observations were carried out as part of the COS Guaranteed Time program (PI: J. Green; PIDs: 11533, 12036), the Disks, Accretion, and Outflows (DAO) of T Tau stars program (PI: G. Herczeg; PID: 11616), and Project WHIPS (Warm H_2 In Protoplanetary Systems; PI: K. France; PID: 12876). The *HST*-COS observations were acquired with both the G130M and G160M gratings for all systems, providing wavelength coverage over the same range of FUV wavelengths (~1100–1700 Å) as the spectra obtained for the five Lupus disks. Spectral features from these data (e.g., emission line strengths, accretion rates) have previously been analyzed in a number of papers, including Yang et al. (2012), Ardila et al. (2013), Ingleby et al. (2013), France et al. (2011b, 2012, 2014, 2017), and references therein. We mirror the techniques described in those works to identify various properties in the new Lupus spectra, reporting uniform measurements over the entire Lupus/Taurus-Auriga disk sample.

2.4. Uncertainty in Literature Measurements of A_V

Observations at FUV wavelengths are highly affected by the amount of dust and gas along the line of sight to a disk (A_V), making accurate reddening corrections critical in interpreting the spectral features. France et al. (2017) report a statistically significant positive correlation between A_V (derived from, e.g., broadband color excesses, deviations from stellar photospheric templates; Kenyon & Hartmann 1995; Hartigan & Kenyon 2003) and the total luminosity from UV-fluorescent H_2. The trend implies that more molecular gas emission is seen from disks with more intervening material; however, there is no physical or chemical process that would produce such a relationship between circumstellar and interstellar material, making systematic overestimates in the A_V measurements a more likely driver. This effect must be removed in order to accurately assess relationships between the UV spectral features.

To provide an estimate of the line-of-sight interstellar extinction that is less sensitive to the circumstellar dust properties, McJunkin et al. (2014) used observed Lyα profiles to directly measure the amount of neutral hydrogen (H I) along the line of sight. The A_V values were then calculated as $A_V/R_V = N(\mathrm{H\,I})/(4.8 \times 10^{21}\,\mathrm{atoms\,cm^{-2}\,mag^{-1}})$ (Bohlin et al. 1978). France et al. (2017) find that the correlation between A_V and $L(H_2)$ becomes statistically insignificant when the McJunkin et al. (2014) reddening values are adopted, so we adopt the H I-derived A_V values for the analysis presented here.

Extinctions derived using the McJunkin et al. (2014) method are typically significantly lower than reported in the literature, since the measurements isolate interstellar $N(\mathrm{H\,I})$ from circumstellar material that may significantly increase A_V estimates (e.g., DR Tau; $\Delta A_V \sim 2.7$). Figure 2 compares the FUV continuum luminosities calculated with $N(\mathrm{H\,I})$-based A_V values to the measurements using more traditional methods to estimate A_V, using targets from McJunkin et al. (2014) and France et al. (2017). We find that the two luminosities are roughly consistent for most disks, demonstrating that the trends presented later in this work are independent of the choice of A_V. Figure 2 also presents the same comparison for Lyα luminosities measured using the two different A_V values, showing just five major outliers that have the largest changes in A_V as well ($\Delta A_V > 0.8$). Of these outliers, only DR Tau is included in the sample we analyze in this work, and all other targets have $\Delta A_V < 0.8$. We therefore conclude that the trends in Lyα emission presented here are also not driven by the choice of A_V.

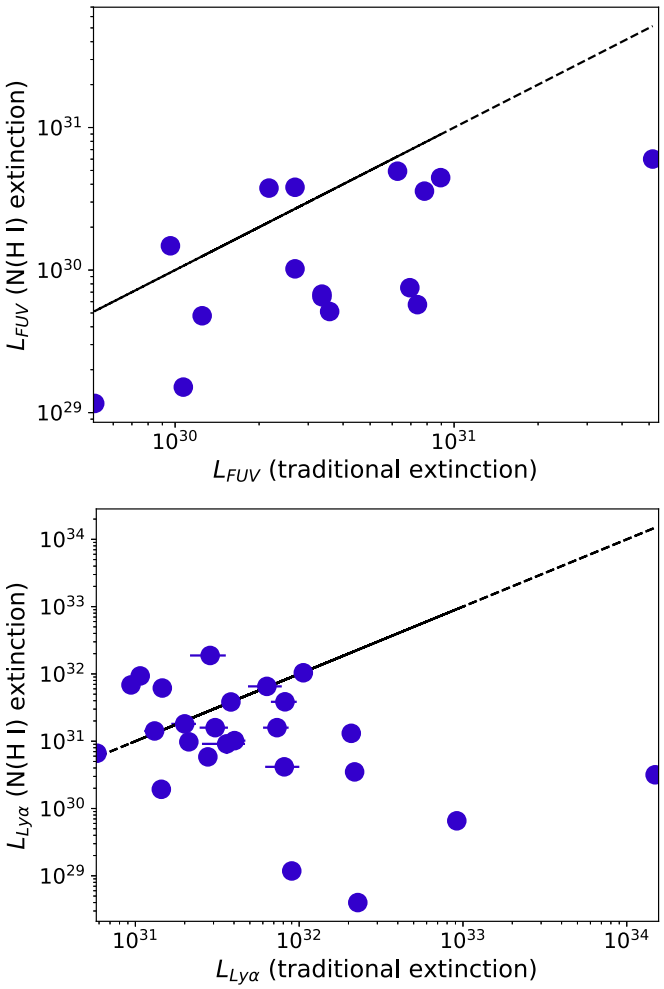

Figure 2. Comparison of luminosities from the FUV continuum (top) and Lyα (bottom), calculated using different values of A_V to deredden the spectrum. The method described in McJunkin et al. (2014), which uses the Lyα wings to estimate $N(\mathrm{H\,I})$ along the line of sight, typically yields smaller A_V and lower luminosities than A_V derived from broadband color excesses or comparisons to stellar photospheric templates (one-to-one relationship traced by black, dashed lines). The major outliers in the bottom panel are disks with A_V values that changed by $\Delta A_V > 0.8$. Since the $N(\mathrm{H\,I})$-based measurements alleviate the correlation between A_V and total flux from UV-H_2 (France et al. 2017), we adopt those extinctions for the analysis presented here.

2.5. Normalized UV Luminosities

Models of UV-sensitive molecular gas distributions have included a broad range of stellar blackbody temperatures, UV

excesses due to accretion, and total UV luminosities, allowing the authors to isolate the impact of UV irradiation from disk geometric properties such as disk mass, flaring angle, and pressure scale height (see, e.g., van Zadelhoff et al. 2003; Walsh et al. 2015; Cazzoletti et al. 2018; Bergner et al. 2019). Other observational work has split the targets by spectral type, allowing the authors to roughly correct for stellar mass and temperature (Pascucci et al. 2009). However, the sample we present here is too small to meaningfully bin the data by both disk and stellar properties. Instead, we divide the individual UV components by the total UV luminosity ($L_{\rm UV,total}$), defined as the sum of fluxes from the FUV continuum, Lyα, UV-H_2, C IV, and C II].

Since both $L_{\rm UV,total}$ and fluxes from the individual UV components are impacted by target properties in the same way (e.g., i_d, M_*), this correction allows us to evaluate the entire sample without binning the data based on disk or stellar parameters. The normalization also reduces the impact of systematic uncertainties in measuring A_V, as described in Section 2.4, although we note that resonant scattering effects may preferentially enhance Lyα fluxes in deeper layers of the disk (see, e.g., Bethell & Bergin 2011), relative to emission at other FUV and NUV wavelengths. When the data were analyzed before accounting for the diversity of disk and stellar parameters, no correlations were observed between any of the UV tracers and the 14 μm HCN or submillimeter CN fluxes. We therefore conclude that normalizing the UV luminosities allows us to provide more physically meaningful information about UV-dependent gas-phase chemistry than using the raw fluxes alone. All plots also differentiate between targets with resolved dust substructure (open markers) and full, primordial disks (filled markers), demonstrating that the results are roughly independent of evolutionary phase.

3. Results

The *HST*-COS and *HST*-STIS spectra described above provide direct measurements of the UV radiation field, which we use to estimate the UV flux reaching the surface of the gas disk. Here, we focus on the role of UV photons in producing CN, which has been detected in ALMA Band 7 observations of a large sample of disks in the Lupus clouds (van Terwisga et al. 2019), including the five studied here. We present the following results under the assumption that the dominant reaction pathway for CN production in disks is

$$\begin{aligned} \mathrm{N} + \mathrm{H_2^*} &\longrightarrow \mathrm{NH} + \mathrm{H} \\ \mathrm{C^+} + \mathrm{NH} &\longrightarrow \mathrm{CN^+} + \mathrm{H} \\ \mathrm{CN^+} + \mathrm{H} &\longrightarrow \mathrm{CN} + \mathrm{H^+}, \end{aligned} \quad (2)$$

where H_2^* is gas that has been pumped into excited vibrational states by FUV photons (Walsh et al. 2015; Heays et al. 2017; Cazzoletti et al. 2018). HCN can then be formed via reactions with H_2 and CH_4

$$\begin{aligned} \mathrm{CN} + \mathrm{H_2} &\longrightarrow \mathrm{HCN} + \mathrm{H} \\ \mathrm{CN} + \mathrm{CH_4} &\longrightarrow \mathrm{HCN} + \mathrm{CH_3} \end{aligned} \quad (3)$$

(Baulch et al. 1994; Walsh et al. 2015; Visser et al. 2018). Destruction of HCN by UV photons also significantly influences the total abundance of CN in the disk (Walsh et al. 2015; Cazzoletti et al. 2018; Pontoppidan et al. 2019), with photodissociation occurring at a rate of 1.6×10^{-9} s^{-1} under a typical interstellar radiation field and a rate of 5.3×10^{-9} s^{-1} under a standard T Tauri Lyα profile (van Dishoeck et al. 2006; Heays et al. 2017). Although the UMIST Database for Astrochemistry (McElroy et al. 2013) lists many other reactions for CN formation, physical–chemical models demonstrate that the H_2^* pathway is the most important route (see, e.g., Visser et al. 2018). This may be attributed to the high abundance of H_2 in disks, relative to molecular species like C_2H and OH that are required for alternate pathways (Visser et al. 2018).

3.1. Photodissociation of N_2 by the FUV Continuum

Gas-phase chemical models of protoplanetary disks find that column densities of nitrogen-dependent molecular species (e.g., CN, HCN) vary with the total FUV flux at the disk surface (Pascucci et al. 2009; Walsh et al. 2012, 2015). The trend is attributed to photoabsorption, since five excited electronic transitions of N_2 fall between 912 and 1100 Å. Absorption at these wavelengths produces predissociated N_2 via coupling to the continuum (Li et al. 2013; Visser et al. 2018). As shown in Equation (1), the atomic nitrogen products react with H_2^* to produce NH, therefore catalyzing formation of molecules like CN and HCN (Walsh et al. 2015; Cazzoletti et al. 2018).

The predicted relationship between molecular abundances and UV irradiation is corroborated by observational studies at IR wavelengths, which find that disks around cool M stars show less emission from nitrogen-bearing molecules than disks around hotter solar-type stars (Pascucci et al. 2009, 2013; Najita et al. 2013). The difference is attributed to varying UV photon production rates, which are expected to be lower in cooler stars (van Zadelhoff et al. 2003; Walsh et al. 2012, 2015). To further investigate this relationship from an observational perspective, we compare CN fluxes measured from ALMA observations (van Terwisga et al. 2019) to FUV fluxes from the *HST*-COS and *HST*-STIS spectra presented here.

Although our *HST* data are truncated below 1000 Å, the method from France et al. (2014) was used to estimate the FUV continuum at shorter wavelengths. The extrapolation was performed on binned fluxes, which were calculated in 210 line-free regions from the longer wavelength data. The continua were fitted with a second-order polynomial and extended down to 912 Å. For uniformity with the larger sample presented in France et al. (2014), we report the total integrated flux from wavelengths <1650 Å and compare these FUV continuum luminosities to both CN and HCN emission (see Figure 3).

We report a significant positive correlation between the FUV and IR HCN fluxes ($\rho = 0.64$; $p = 0.01$), a trend that is consistent with model predictions. An analysis of the H-leverage values and studentized residuals for a linear regression model of the form $L_{\rm HCN} = m \times L_{\rm FUV}/L_{\rm UV,total} + b$ shows that the DR Tau and AA Tau (2013) spectra are highly influential data points. When these outliers are removed from the correlation, the Spearman rank coefficient increases to $\rho = 0.66$, although p remains at 0.01 because of the reduction in sample size. Both targets are included in Figure 3, but we note that the AA Tau (2013) spectrum in particular is impacted by an inner disk warp (Hoadley et al. 2015; Schneider et al. 2015; Loomis et al. 2017) that is attenuating the FUV flux. In contrast with both the HCN results and modeling work, we find a significant negative correlation between the FUV and submillimeter CN fluxes

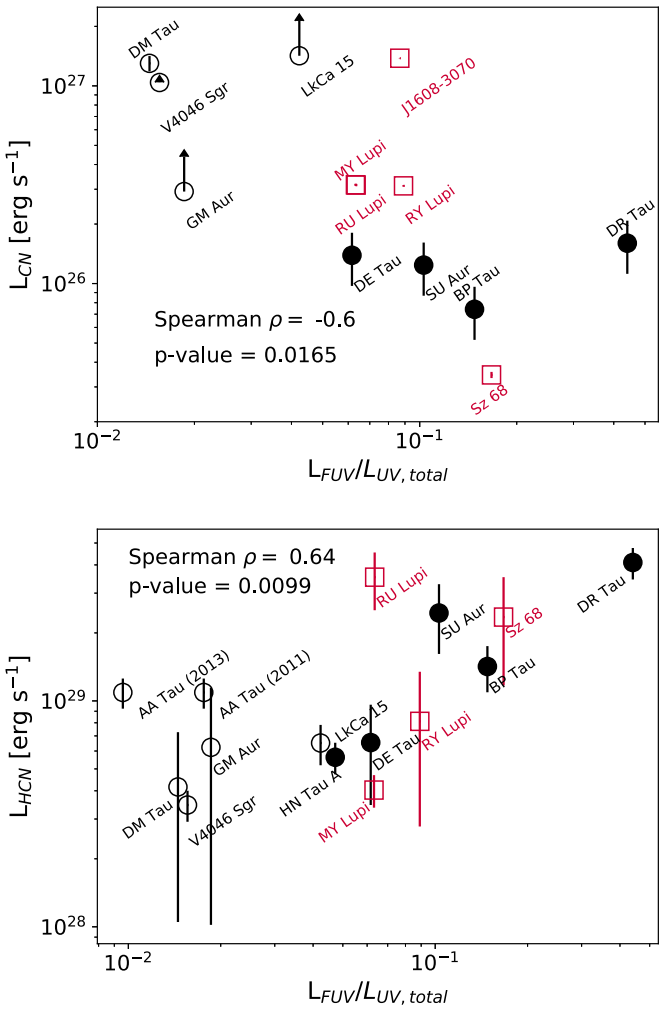

Figure 3. Submillimeter CN (top) and 14 μm HCN (bottom) luminosities vs. fractional flux from the FUV continuum (integrated from 912 to 1650 Å). The five Lupus systems are shown as red squares and the subset of disks from France et al. (2017) as black circles, with open markers representing disks with resolved dust substructure. N_2 molecules are readily predissociated by photons between 912 and 1000 Å (Li et al. 2013), and the atomic nitrogen then reacts with H_2^* as a first step in CN formation (Walsh et al. 2015; Cazzoletti et al. 2018). These two relationships demonstrate that while N_2 photodissociation may proceed more efficiently in disks that are more strongly irradiated by FUV photons relative to the rest of the UV spectrum, CN photodissociation may increase as well. Measured FUV luminosities in this plot are accurate to within a factor of ~1.5–2, with the choice of A_V dominating the uncertainties.

($\rho = -0.6$; $p = 0.02$) that points to increased photodissociation of CN in disks with strong FUV irradiation. Both DR Tau and AA Tau are once again the most influential data points.

The degeneracy between gas column densities and temperature of the emitting region makes it difficult to conclusively determine whether the observed trends are due to efficient molecule formation/destruction pathways or increased emission from warmer disks. The negative correlation between submillimeter CN emission and the FUV continuum implies that this trend at least is dominated by photodissociation, since increased UV irradiation could lead to a warmer disk and therefore an opposite relationship. However, the trend of increased IR HCN emission in systems with stronger FUV fluxes could be attributed to either scenario, with both a larger number of HCN molecules and higher temperatures leading to enhanced populations in the upper state of the 14 μm transition. This result will become easier to interpret as more measurements of submillimeter HCN emission (see, e.g., Öberg et al. 2010, 2011; Bergner et al. 2019) are acquired with ALMA in coming years. Despite the uncertainty in the driving force behind the HCN trend, the negative and positive correlations between the FUV continuum and CN and HCN, respectively, demonstrate that the amount of FUV flux in a given disk helps control the balance of formation and destruction pathways that determine abundances of UV-sensitive species.

3.2. Lyα as a Regulator of Disk Chemistry

Lyα emission is by far the strongest component of the UV radiation field, comprising roughly 75–95% of the total flux from ~912 to 1700 Å in typical accreting T Tauri systems (Bergin et al. 2003; Herczeg et al. 2004; Schindhelm et al. 2012b; France et al. 2014). Its broad width in wavelength space encompasses transitions of a variety of molecules, including electronic transitions of H_2 (Herczeg et al. 2002, 2004; Hoadley et al. 2017) and CO (France et al. 2011b; Schindhelm et al. 2012a) and photodissociation energies of HCN, C_2H_2 (Bergin et al. 2003; Walsh et al. 2015; Heays et al. 2017), and H_2O (France et al. 2017). Destruction via Lyα photons is not necessarily more efficient than dissociative transitions at other wavelengths, but this is mitigated by the large number of Lyα photons relative to other regions of the UV spectrum. Unfortunately, the observed Lyα feature is always contaminated by geocoronal emission and ISM absorption along the line of sight, making direct measurements difficult. Instead, we use the method from Schindhelm et al. (2012b) to reconstruct the Lyα profiles for the five Lupus disks from observations of UV-fluorescent H_2.

UV-H_2 fluorescence is activated when a population of hot, vibrationally excited H_2 ($T > 1500$ K; Black & van Dishoeck 1987; Ádámkovics et al. 2016) is "pumped" from the ground electronic state ($X^1\Sigma_g^+$) into the first and second dipole-allowed excited electronic state ($B^1\Sigma_u^+$, $C^1\Pi_u$) by photons with energies that fall along the Lyα line profile (Herczeg et al. 2002, 2004; France et al. 2011a). A cascade of UV emission lines is then observed as the molecular gas population transitions back to the ground electronic state. The features can be divided into groups called progressions, where a single progression, denoted [ν', J'], consists of all transitions out of the same upper electronic level with vibrational state ν' and rotational state J' (Herczeg et al. 2002, 2004). We measured fluxes from the strongest emission lines in 12 progressions (see Table 2 of France et al. 2012) by integrating over models of a Gaussian profile convolved with the *HST*-COS line-spread function (LSF) and superimposed on a linear continuum. Upper limits on features indistinguishable from the continuum were calculated as the rms flux within a 3 Å range across the expected line center. The total progression fluxes ($F_{H_2,i}$) were then used as Lyα "data" (y), where the x value for each data point is the Lyα pumping wavelength for the electronic transition. We then fit a model Lyα profile to the $(x_i, y_i) = (\lambda_{LyA,i}, F_{H_2,i})$ data points.

The Lyα model consists of an initial "intrinsic" Gaussian emission line, an H I outflow between the star/accretion shock and the molecular gas disk, and a population of H_2 that absorbs the Lyα photons. We allow five model parameters to vary: the amplitude of the intrinsic profile ($I_{Ly\alpha}$), the velocity and column density of the outflowing H I (v_{out}, N_{out}), and the temperature and column density of the absorbing H_2 (T_{H_2}, N_{H_2}). The FWHM

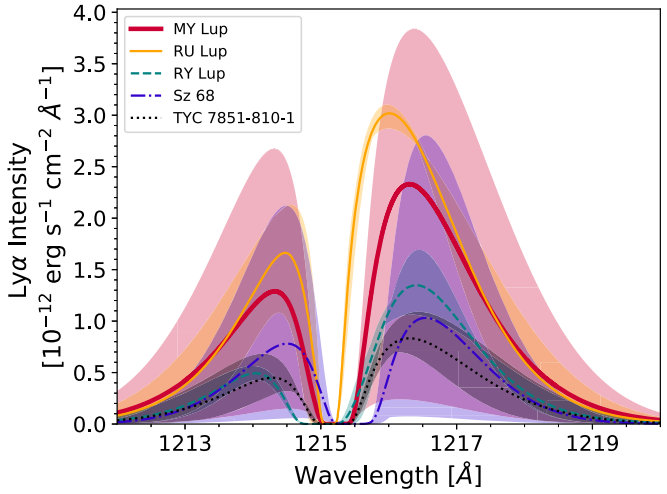

Figure 4. Comparison of the reconstructed Lyα profiles at the disk surface for all five Lupus targets in our sample, with colored contours showing rough uncertainties associated with the modeling procedure. Reconstruction is done using observed UV-H_2 emission lines as data points (Schindhelm et al. 2012b), since molecules are pumped into these excited electronic states by Lyα photons. Absorption seen on the blue side of the line profiles is due to an atomic outflow between the star and disk, rather than interstellar H I along the line of sight.

of the intrinsic profile for each system was fixed to the average, maximum, and minimum values from Schindhelm et al. (2012b), resulting in three model profiles for each target. Posterior distributions for the model parameters were constructed using MCMC sampling (Foreman-Mackey et al. 2013) within the bounds defined by Schindhelm et al. (2012b). However, we find that the model uncertainties are better captured by the variations in the average, maximum, and minimum FWHM profiles. Figure 4 shows the median Lyα profile at the disk surface for all five Lupus systems, with colored contours representing the bounds set by the three FWHM values (see Table 4).

We compare the total luminosities from our reconstructed Lyα profiles to the the CN and HCN luminosities in Figure 5. Since CN molecules can also form as byproducts of HCN or CH_3CN photodissociation (Walsh et al. 2015) via Lyα photons near 1216 Å (Nuth & Glicker 1982; Bergin et al. 2003), we expect that increased Lyα irradiation of the disk surface will increase the significance of dissociative pathways in regulating both CN and HCN column densities. However, no statistically significant relationships are detected between Lyα and either HCN ($\rho = -0.4$; $p = 0.10$) or CN ($\rho = 0.38$; $p = 0.17$). We do note that the Spearman rank coefficients themselves (ρ) are consistent with model predictions, with increased CN and decreased HCN emission observed from targets with stronger Lyα emission.

Since the Lyα profiles are derived from UV-fluorescent H_2^*, the lack of correlation between CN and Lyα emission may be attributed to the radial stratification of the UV-H_2 and submillimeter CN. The UV-H_2 emission originates from gas in surface layers of the inner disk ($r < 10$ au), while the CN population extends to radii of ~30–50 au in the outer disk (Bergner et al. 2019; van Terwisga et al. 2019). Similarly, vertical stratification may be responsible for the null relationship between HCN emission and Lyα emission, with UV-H_2 emission originating from much closer to the disk surface than the 14 μm HCN features. A direct comparison between observed Lyα, HCN, and CN luminosities likely requires more careful treatment of optical depth effects. Furthermore, a bootstrapping analysis of the data returns $\pm 1\sigma$ confidence intervals on the Spearman rank coefficients of [−0.71, −0.29] and [0.2, 0.67] for the HCN and CN versus $L(\mathrm{Ly}\alpha)/L(\mathrm{UV, total})$ correlations. Although the upper limits of the confidence intervals are consistent with robust linear relationships, it is possible that targets with larger uncertainties on the reconstructed Lyα profiles (e.g., MY Lupi, Sz 68) are masking underlying trends in the data.

We also note that the *HST*-COS, *Spitzer*-IRS, and submillimeter CN observations were not conducted simultaneously (see Tables 2, 3), implying that the reconstructed Lyα profiles may not be representative of the flux reaching the disk surface at the time of the molecular gas observations. However, an *HST* analysis of older K and M dwarfs has demonstrated that Lyα line strengths do not increase as much as other atomic features during flares (e.g., Si IV λ1400; Loyd et al. 2018), perhaps indicating that Lyα emission also remains steady during typical YSO variability. Although France et al. (2011a, b) report a strong correlation between the FUV continuum and the C IV λ1550 fluxes that are often used as a proxy for mass accretion rate, multiple phased observations of a single target are likely required to determine whether the FUV continuum also fluctuates with accretion rate during periods of variability. Such observations will be acquired in the next few years through the Ultraviolet Legacy Library of Young Stars as Essential Standards (ULLYSES)[9] Director's Discretionary program on *HST*.

3.3. Mapping the Population of H_2^*

3.3.1. Lyα-pumped H_2

As introduced in Section 3.2, we detect a suite of emission lines from hot ($T \sim$ 1500–2500 K; Ádámkovics et al. 2016), fluorescent H_2 in the *HST*-COS spectra of all five disks. Although our *HST*-COS spectra are not spatially resolved, *HST*-STIS spectra of the same features in the disk around TW Hya show that the H_2 emission must be within ~2 au of the central star (Herczeg et al. 2004). The features may therefore provide constraints on the distribution of H_2^* available for CN and HCN formation in the inner disk region. Figure 6 provides a cartoon demonstrating the rough spatial locations of the emitting gas.

The UV-H_2 emission lines are spectrally resolved (i.e., broader than the *HST*-COS resolution), allowing us to extract information about the spatial distribution of hot, fluorescent gas. Assuming that the material is in a Keplerian disk, the FWHMs of the emission lines can be mapped to an average radial location as

$$\langle R_{\mathrm{H_2}} \rangle = GM_* \left(\frac{2 \sin i}{\mathrm{FWHM}} \right)^2 \quad (4)$$

(Salyk et al. 2011a; France et al. 2012), where M_* is the stellar mass and i is the disk inclination. We average the FWHMs of the strongest emission lines from the $[\nu', J'] = [1, 4]$, $[1, 7]$, $[0, 1]$, and $[0, 2]$ progressions, and calculate a radius for each progression (see Table 5), finding that the bulk UV-H_2 emission originates inside ~2 au for all five disks. The most distant emission radii in the [1, 4] and [1, 7] progressions are

[9] http://www.stsci.edu/stsci-research/research-topics-and-programs/ullyses

Table 4
Best-fit Parameters[a] for Lyα Reconstruction

Target	$I_{Ly\alpha}$ (erg s^{-1} cm^{-2} Å^{-1})	v_{out} (km s^{-1})	N_{out} (dex)	T_{H_2} (K)	N_{H_2} (dex)
RU Lupi	$(3.5 \pm 0.5) \times 10^{-12}$	-138^{+6}_{-18}	$18.2^{+0.4}_{-0.2}$	3100 ± 900	$18.2^{+0.5}_{-0.2}$
RY Lupi	$2^{+2}_{-1} \times 10^{-12}$	-162^{+12}_{-6}	$19.1^{+0.4}_{-0.2}$	2000 ± 1000	$18.8^{+1.5}_{-0.5}$
MY Lupi	$3^{+50}_{-30} \times 10^{-13}$	-108^{+50}_{-20}	$18.5^{+0.3}_{-1}$	3000^{+1500}_{-900}	19.5 ± 2
Sz 68	$1^{+50}_{-4} \times 10^{-13}$	-60^{+30}_{-100}	18 ± 1	4000 ± 1000	$20.5^{+1.5}_{-3}$
J1608-3070	$1.1^{+0.4}_{-0.1} \times 10^{-12}$	-114^{+1}_{-11}	$18.9^{+0.9}_{-0.1}$	3100^{+400}_{-200}	18^{+2}_{-1}

Note.
[a] Model parameters are: $I_{Ly\alpha}$ = amplitude of intrinsic Lyα profile, v_{out} = velocity of intervening outflowing gas, N_{out} = column density of intervening outflowing gas, T_{H_2} = temperature of fluorescent H_2, N_{H_2} = column density of fluorescent H_2. The FWHM of the intrinsic profile for each system was held constant in the model, set to the average (708 km s^{-1}) from Schindhelm et al. (2012b). Error bounds on the parameters were estimated by running the model with the FWHM fixed to the minimum (573 km s^{-1}) and maximum (912 km s^{-1}) values from that work.

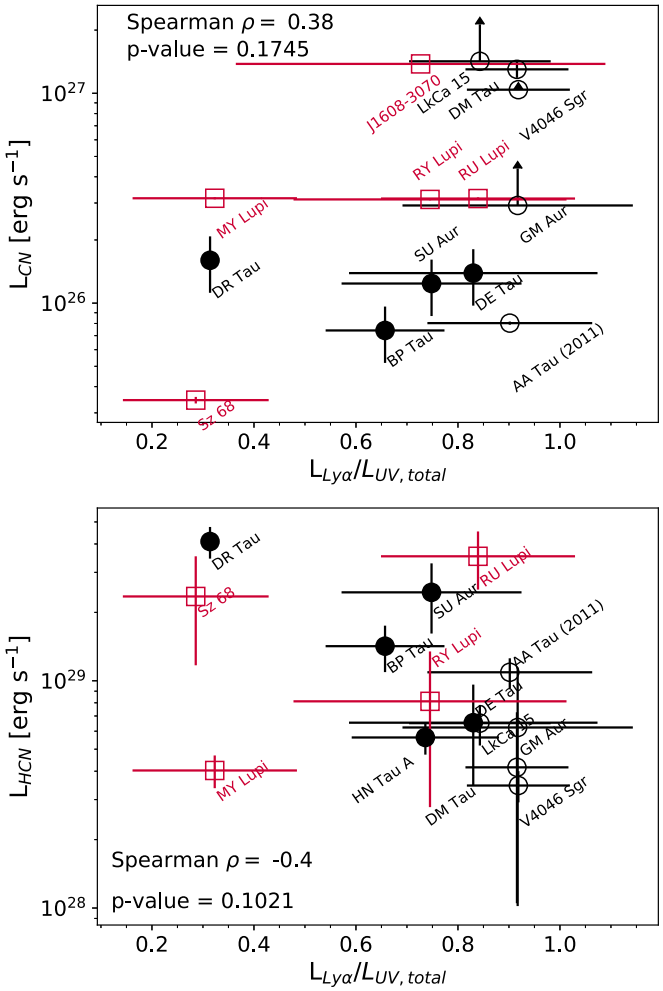

Figure 5. Submillimeter CN (top) and 14 μm HCN (bottom) emission vs. fractional Lyα luminosity. Lupus disks are shown as red squares and systems from France et al. (2017) as black circles, with open markers representing systems with resolved dust substructure. Neither species is significantly correlated with Lyα emission, but the Spearman rank coefficients are tentatively consistent with models predicting increased CN and decreased HCN abundances with increased Lyα irradiation. The 2013 AA Tau spectrum is omitted from these plots, because the Lyα fluxes were very similar to the spectrum from 2011.

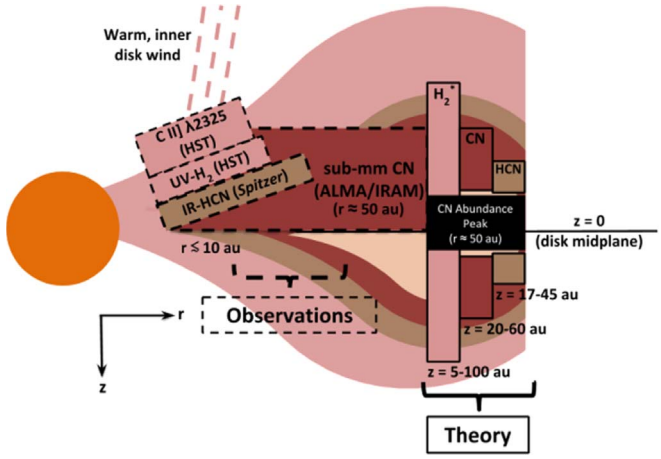

Figure 6. Rough spatial locations of emitting gas that produces C II] λ2325, UV-H_2, IR-HCN, and submillimeter CN emission lines, compared to radius where physical–chemical models predict peak abundances of H_2^*, CN, and HCN (Cazzoletti et al. 2018). Observed gas populations should overlap at radii close to the central star, although the submillimeter CN emission is the only component that generally extends across the full disk.

measured for J1608-3070, which has the largest submillimeter dust cavity ($r \sim 75$ au; van der Marel et al. 2018). This is consistent with the results of Hoadley et al. (2015), who found that disks with less advanced dust evolution typically have broad UV-H_2 features that are dominated by gas located close to the star. Although resonant scattering should allow pumping photons from the Lyα line wings to penetrate deeper into the disk than those from the line center (Bethell & Bergin 2011), we find no trends between the average emitting radius calculated for each progression and the Lyα pumping wavelength responsible for exciting the transitions.

Since H_2^* is required to produce CN (see Equation (1)), the UV-H_2 features are a probe of the uppermost layer of available reactants located at the average radius of emitting gas (R_{H_2}). We explore this relationship by comparing the CN and HCN luminosities to the total flux from fluorescent UV-H_2 emission lines (see Figure 7), finding that neither species is correlated with the UV-H_2. In the case of HCN, the scatter can be attributed to the vertical stratification effects discussed in Section 3.2, since the H_2^* and HCN abundances are expected to peak at different heights relative to the disk midplane (Cazzoletti et al. 2018). Lyα photons are only able to pump H_2^* in a thin surface layer, so the UV-H_2 features do not contain information from vibrationally excited gas present deeper in the disk that would be collocated with the HCN. By contrast, the submillimeter emission traces CN molecules in the cold outer disk, where

Table 5
Average Emission Radii of Hot, Fluorescent H_2

Target	FWHM$_{[1,4]}$ (km s^{-1})	$\langle R_{H_2}\rangle_{[1,4]}$ (au)	FWHM$_{[1,7]}$ (km s^{-1})	$\langle R_{H_2}\rangle_{[1,7]}$ (au)	FWHM$_{[0,1]}$ (km s^{-1})	$\langle R_{H_2}\rangle_{[0,1]}$ (au)	FWHM$_{[0,2]}$ (km s^{-1})	$\langle R_{H_2}\rangle_{[0,2]}$ (au)
RU Lupi	51 ± 1	0.10 ± 0.03	49 ± 2	0.11 ± 0.03	31 ± 2	0.29 ± 0.08	50 ± 3	0.11 ± 0.03
RY Lupi[a]	53.3 ± 0.7	1.8 ± 0.5	51 ± 1	2.0 ± 0.5	63 ± 10	1 ± 1	45 ± 4	2.6 ± 0.8
MY Lupi	48 ± 1	1.4 ± 0.2	46 ± 2	1.5 ± 0.2	48 ± 1	1.4 ± 0.2	59 ± 3	0.9 ± 0.1
Sz 68	57 ± 2	0.5 ± 0.3	57 ± 5	0.5 ± 0.3	57 ± 5	0.5 ± 0.4	43 ± 3	0.8 ± 0.6
J1608-3070	47.1 ± 0.7	2 ± 1	42.5 ± 0.7	3 ± 2	77 ± 10	0.8 ± 0.4	75 ± 10	0.8 ± 0.4

Note.
[a] The FWHMs listed here for RY Lupi are from single-component fits to the emission lines. Arulanantham et al. (2018) presents a more detailed analysis of the H_2 line shapes, showing that the strongest features in the [1, 4] progression are better fit by a two-component model. We also adopt the disk inclination from van der Marel et al. (2018) (68°), instead of the scattered light inclination from Manset et al. (2009) (85.°6).

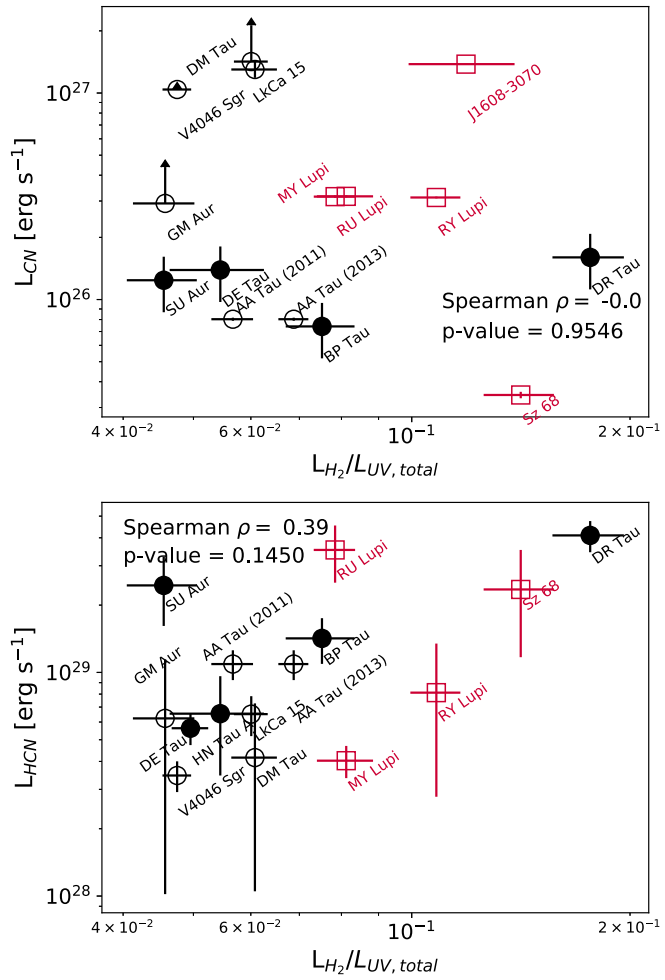

Figure 7. CN and HCN luminosities vs. fractional luminosity from UV-pumped H_2, with open markers representing disks with resolved dust substructure (i.e., rings, gaps, or cavities). Lupus disks are shown as red squares, while the black circles are systems from France et al. (2017). Neither submillimeter CN nor IR HCN is significantly correlated with UV-H_2, which is likely due to the disparate radial and vertical stratification of the three populations of emitting gas.

the population of H_2^* declines due to extinction of pumping photons from the UV continuum (Cazzoletti et al. 2018; Visser et al. 2018). The radial distribution of UV-H_2 may provide estimates of either how far Lyα emission is able to travel in the disk or a rough boundary for the population of H_2^*. We explore this degeneracy further in Section 4 by using 2D radiative transfer models to reproduce the UV-H_2 emission lines.

3.3.2. 1600 Å "Bump" as a Signature of H_2O Dissociation

Previous studies of UV continuum emission from young stars with disks have identified an excess "bump" in the spectra around ∼1600 Å (Bergin et al. 2004; Herczeg et al. 2004). The feature is attributed to continuum and line emission from Lyα-pumped H_2^*, where the population of H_2^* is indirectly produced during H_2O dissociation in the inner disk ($r < 2$ au; France et al. 2017). While the Lyα and bump luminosities are strongly correlated ($\rho = 0.74$, $p = 1.72 \times 10^{-3}$; France et al. 2017), no relationship is observed between the bump and X-ray luminosities (Espaillat et al. 2019). This implies that Lyα photons may play a more prominent role than the X-ray radiation field in regulating the distribution of hot H_2O and vibrationally excited H_2 at radii close to the central star.

We use the method described in France et al. (2017) to measure bump fluxes and calculate luminosities for the three disks in our sample that were not included in that work. A second-order polynomial fit to the FUV continuum, representative of the underlying flux, was integrated from 1490 to 1690 Å and subtracted from the total observed flux in the same wavelength region. The residual flux can be attributed to the bump alone (see Table 6). Figure 8 compares the CN/HCN and bump luminosities, again showing no clear linear trend between the spectral features. Similar to the Lyα-pumped fluorescent gas, the H_2^* responsible for producing the bump is therefore likely located higher in the disk surface than the 14 μm HCN and constrained to closer radii than the submillimeter CN.

3.4. C II] λ2325 Emission as a Tracer of Inner Disk C^+

The semi-forbidden C II] emission lines at λ2325 are detected in all the Lupus and Taurus-Auriga targets with *HST*-STIS spectra. Models of the feature in other young systems find that its shape is consistent with an origin at the base of a warm, inner disk ($r \sim 0.1$–1 au) wind, coincident with surface layers of the disk itself (Gómez de Castro & Ferro-Fontán 2005) and with similar formation conditions to the [O I] 6300 Å line (Simon et al. 2016). Studies of the [O I] line show that the profile is narrower in systems with dust-depleted inner disks (Simon et al. 2016; Banzatti et al. 2019), indicating that the base of the wind, and therefore all the emitting gas it contains, shifts to more distant radii within the disk. C II] therefore may also be an important observational proxy for the population of inner disk C^+.

Simon et al. (2016) find that the low-velocity component of the [O I] profile is consistent with Keplerian rotation, with

Table 6
Hot Gas and Stellar Luminosities

Target	L_{H_2} (10^{30} erg s^{-1})	$L_{1600\ Å}$ (10^{29} erg s^{-1})	$L_{Ly\alpha}$ (10^{29} erg s^{-1})	$L_{C\ II}$ (10^{29} erg s^{-1})	L_{FUV}[a] (10^{29} erg s^{-1})
RU Lupi	6.1 ± 0.4	5.54 ± 1.59[b]	170 ± 70	···	49.4[b]
RY Lupi	1.01 ± 0.08	1.55 ± 0.8[b]	70 ± 25	2.18 ± 0.02	8.3
MY Lupi	0.45 ± 0.04	15.3 ± 6	18[c]	0.69 ± 0.01	3.5
Sz 68	0.27 ± 0.03	3.1 ± 1	5[c]	0.73 ± 0.01	3.2
J1608-3070	0.6 ± 0.1	1.7 ± 0.7	37[c]	0.18 ± 0.01	4.4

Notes.
[a] FUV continuum luminosities are accurate to within a factor of ∼1.5–2.
[b] Values from France et al. (2017).
[c] Reconstructed Lyα profiles have large uncertainties, due to noisy UV-H_2 emission lines.

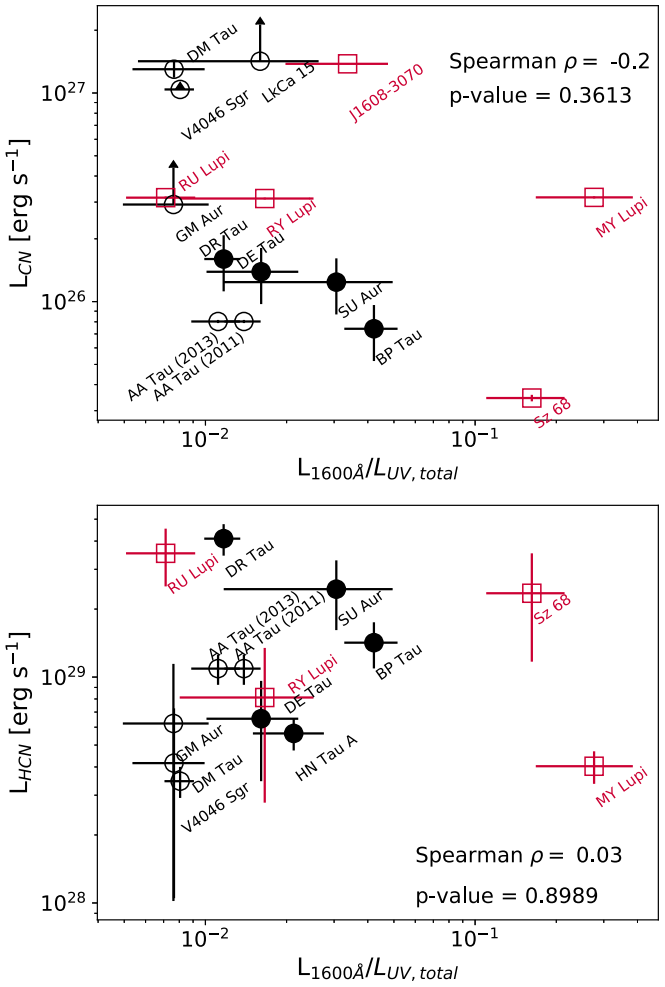

Figure 8. CN and HCN luminosities vs. fractional luminosity from the 1600 Å bump (produced by Lyα-pumped H_2^* left behind during H_2O photodissociation; France et al. 2017). Lupus disks are shown as red squares, while the black circles are systems from France et al. (2017). Strength of the bump is correlated with time-varying accretion luminosities (Espaillat et al. 2019), implying that the measurements shown here are snapshots of the population of hot, nonthermal gas and not necessarily reflective of equilibrium chemical conditions.

emitting gas originating in radially separated components located between 0.05 and 5 au. Only one target (AA Tau) in the sample presented here was observed at high enough spectral resolution and signal-to-noise to obtain kinematic information from the C II] emission, with three individual features resolved at λ2325.40, λ2326.93, and λ2328.12 Å. We find that the central feature (λ2326.93 Å) has a similar FWHM to the broad component of the [O I] 6300 Å line (96 km s^{-1}; Banzatti et al. 2019), which likely implies that the two emission lines have similar inner disk origins. The C II] λ2325 emission is also correlated with the ionization fraction derived from carbon recombination lines (e.g., DR Tau; McClure 2019), providing further support that the two features come from a roughly cospatial population of inner disk gas.

Ionized carbon (C^+) is a key reactant in the main formation pathways of C_2H (Henning et al. 2010; Walsh et al. 2015; Miotello et al. 2019) and CN (Walsh et al. 2015; Cazzoletti et al. 2018; Visser et al. 2018). C^+ also plays an important role in CO_2 destruction, with physical–chemical models showing an enhancement in the CO_2 column density at $r \sim 10$ au, where gas self-shielding allows the C^+/C ratio to drop below unity (Walsh et al. 2012). We note that the FUV C II λ1335 resonant feature is also included in the data sets presented here. However, its line profiles are likely dominated by the accretion preshock region and protostellar chromosphere and consistently show detectable wind absorption signatures (Johns-Krull & Herczeg 2007), requiring a more complicated method to untangle the associated population of C^+ that is directly involved in molecule formation and destruction than needed for the C II] λ2325 feature.

To explore whether the C II] emission is related to the CN and HCN observations, C II] line fluxes were measured for each target in our sample by integrating the dereddened *HST*-STIS spectra over a wavelength range spanning all three C II] features and subtracting a linear continuum (see Table 5). Figure 9 compares the CN, HCN, and C II] λ2325 luminosities, showing statistically significant relationships between the relative fluxes from C II] and emission from both molecular species. We find that HCN emission is stronger in systems with higher C II] fluxes ($\rho = 0.82$; $p = 0.0005$), although CN emission appears to decline as C II] fluxes increase ($\rho = -0.5$; $p = 0.03$). However, we note that the CN relationship is largely driven by GM Aur and SU Aur, which both have high H-leverage values and studentized residuals when included in a linear regression model of the form $L_{CN} = m \times L_{C\,II]}/L_{UV,total} + b$.

The negative correlation between fractional C II] and submillimeter CN emission points to a relationship between C II] λ2325 emission and the FUV continuum (see Figure 10), implying that more CN is photodissociated in systems with stronger FUV fluxes and correspondingly larger C II] fluxes. Since the FUV continuum is strongly associated with accretion (France et al. 2014), we explore whether the population of C^+ is similarly driven. Although we find that the C II] emission is

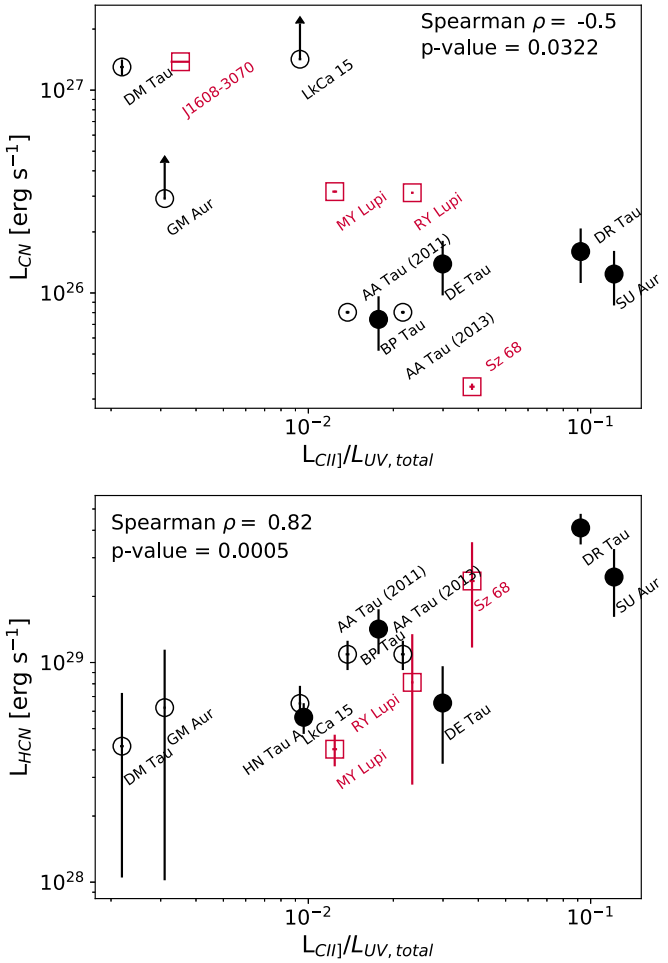

Figure 9. HCN and CN luminosities vs. fractional C II] λ2325 emission. The five Lupus systems are shown as red squares and the subset of disks from France et al. (2017) as black circles, with open markers representing disks with resolved dust substructure. The submillimeter CN emission is negatively correlated with the C II] feature, and a strong positive correlation is seen with the IR HCN emission. The relationships can likely be attributed to accretion processes that enhance both C II] and HCN emission and dissociate CN.

not significantly correlated with the mass accretion rate ($\rho = 0.33$; $p = 0.26$), the positive relationship between C II] and the FUV continuum may still be a byproduct of accretion-related processes that are difficult to trace without contemporaneous measurements of mass accretion rates and C II] fluxes. Since only a handful of targets presented here have high-resolution *HST*-STIS observations of the C II] λ2325 feature, a more detailed kinematic analysis of the line properties is outside the scope of this work.

4. Discussion

Physical–chemical models of disks have suggested that emission from Lyα and the FUV continuum directly impact molecular gas abundances, providing photons at the energies required for gas-phase reactions to proceed. Although we find significant correlations between both 14 μm HCN and submillimeter CN and the FUV continuum, neither species appears to be related to Lyα emission. In order to understand this discrepancy, we examine the impact of disk geometry on the observed spectra and consider whether the optical depth of the inner disk has a significant impact on our results.

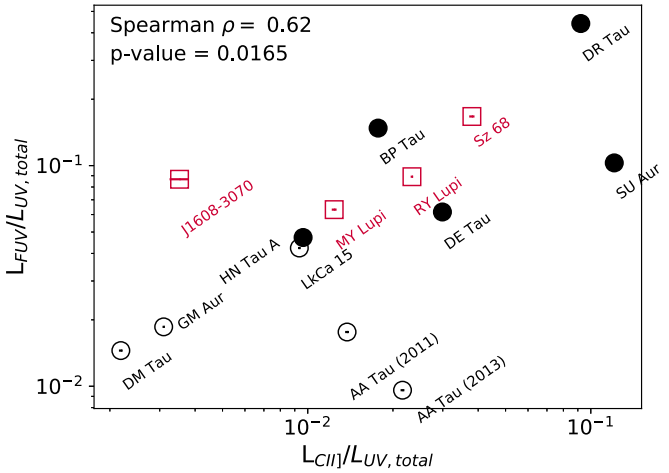

Figure 10. Fractional FUV continuum emission vs. fractional C II] λ2325 luminosities. Both quantities are significantly correlated with 14 μm HCN emission, implying that systems with stronger FUV and C II] fluxes are better able to produce HCN in the inner disk. A full kinematic analysis of the C II] line profiles is likely required to determine whether the C II] emission traces the C^+ population involved in gas-phase chemistry or accretion processes that enhance the strength of the feature.

4.1. Extent of UV-H_2 Emitting Region

UV-H_2 features observed with *HST*-COS are typically much broader than the instrument resolution ($\Delta v \sim 17\,\mathrm{km\,s^{-1}}$), implying that most of the detected flux is emitted at radii $\leqslant$10 au from the central star (see, e.g., France et al. 2012). This is supported by *HST*-STIS spectra of H_2 in the disk around TW Hya, which show that the UV-H_2 emission lines are not spatially extended and are therefore confined to the inner disk (Herczeg et al. 2002). However, physical–chemical models suggest that both Lyα and FUV photons reach large swaths of the outer disk (see, e.g., Cleeves et al. 2016). The FUV photons can pump H_2 into vibrationally excited states at radii where the gas temperature is too low for thermal populations of H_2^* to survive (see, e.g., Cazzoletti et al. 2018). Lyα photons then act as a searchlight illuminating the vibrationally excited population.

Since fluorescent emission is not detected from the outer disk (see Figure 11), the radial extent of the UV-H_2 emitting region may be restricted by either:

1. the extent to which Lyα pumping photons can travel into the disk (Lyα-limited), or
2. the total abundance of H_2^*, excited thermally ($T > 1500$ K) and via FUV-pumping (H_2^*-limited).

The negative correlation between submillimeter CN fluxes and the FUV continuum (measured both directly and via C II] λ2325 emission) reported here implies that UV photons are able to reach the outer disk, perhaps enhancing the population of H_2^* in those regions. With this in mind, we focus on a simple model of the Lyα-limited scenario. A more advanced full disk H_2^* distribution will be analyzed in a future paper on the H_2^*-limited scenario.

4.2. The 2D Radiative Transfer Models of UV-H_2 Emission

To investigate whether our UV-H_2 observations are Lyα-limited, we use the 2D radiative transfer model developed by Hoadley et al. (2015) to reproduce the distributions of fluorescent gas in 4/5 of the Lupus disks presented here. The

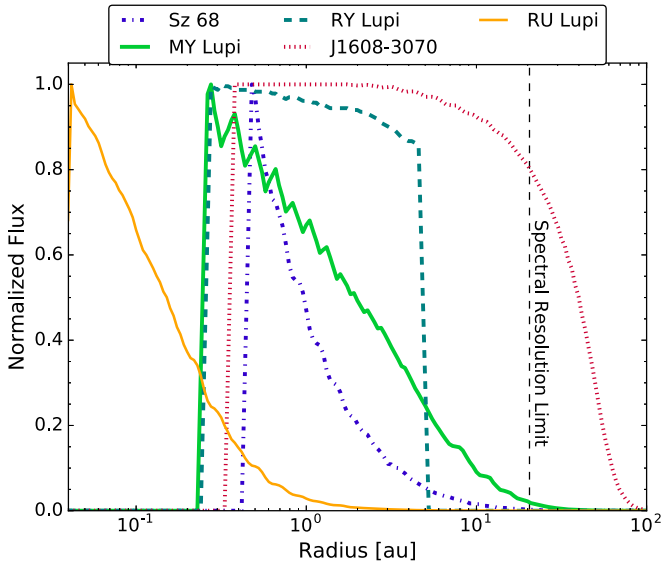

Figure 11. Radial distributions of flux from hot, UV-fluorescent H_2 pumped by Lyα in the five Lupus disks presented here, obtained by fitting a 2D radiative transfer code to individual emission lines. Flux distribution in J1608-3070 extends to much more distant radii than the other three systems, consistent with a depletion of small dust grains inside a large submillimeter cavity ($r_{\rm cav} \sim 75$ au; van der Marel et al. 2018). Although the flux distribution from MY Lupi spans the radii of its first two dust rings ($r \sim 8$, 20 au; Huang et al. 2018), we detect no sign of a break in the population of hot gas. Finally, we note that the flux distribution from Sz 68 is sharply truncated around 10 au, implying that the UV-H_2 emission extends to the edge of the system's circumprimary disk (Kurtovic et al. 2018).

model propagates Lyα photons into a Keplerian disk with a power-law temperature gradient of coefficient q, fixed temperature $T_{1\,\rm au}$ at a radial distance of 1 au, and a minimum $T = 1000$ K for UV-fluorescence,

$$T(r) = T_{1\,\rm au}\left(\frac{r}{1\ \rm au}\right)^{-q}, \tag{5}$$

a pressure scale height dependent on the radial temperature distribution $T(r)$ and stellar mass M_*,

$$H_p(r) = \sqrt{\frac{kT(r)}{\mu m_{\rm H}}\frac{r^3}{GM_*}}, \tag{6}$$

and a surface density distribution with characteristic radius r_c, power-law coefficient γ, and normalization factor $\Sigma_c = M_{\rm H_2}(2-\gamma)/\mu r_{\rm char}(2\pi)^{3/2}$

$$\Sigma(r) = \Sigma_c\left(\frac{r}{r_c}\right)^{-\gamma}\exp\left[-\left(\frac{r}{r_c}\right)^{2-\gamma}\right]. \tag{7}$$

We calculate the mass density distribution at some height z above the disk midplane ($\rho(r, z)$) for the entire volume of H_2 gas and the corresponding number density ($n_{[\nu,J]}(r, z)$) and optical depth ($\tau_\lambda(r, z)$) of molecules in the upper level of each progression. Once the physical structure of the underlying hot H_2 population has been derived, the distribution of UV-H_2 flux from each transition is calculated as

$$F_{\lambda_{\rm H_2}}(r, z) = \eta F_{*,{\rm Ly}\alpha}\left(\frac{R_*^2}{r^2}\right)\left(\frac{(r\cos i_{\rm disk})^2}{s(r, z)^2}\right) \times B_{mn}\sum{}^{'}\tau_\lambda(1 - e^{-\tau'_\lambda(r,z)}), \tag{8}$$

where η represents the geometric fraction of the disk exposed to Lyα photons (held constant at 0.25; Herczeg et al. 2004), $F_{*,{\rm Ly}\alpha}$ is the Lyα flux reaching the gas, B_{mn} is the branching ratio that describes the likelihood of a given transition relative to all other transitions from the same upper level, and $s(r, z)$ is the sightline from the observer to a gas parcel at position (r, z) in the disk. The flux distribution is then summed over the entire disk, producing an emission line profile that we fit directly to the observed UV-H_2 spectra. The resulting model distribution of gas informs us about where in the disk the H_2^* is exposed to Lyα radiation, providing radial constraints on the uppermost layer of reactants for producing CN molecules in the inner disk.

To fit these models to the observed UV-H_2 features from the Lupus disks, we used the reconstructed Lyα profiles shown in Figure 4 to estimate $F_{*,{\rm Ly}\alpha}$ for each progression. The disk inclinations ($i_{\rm disk}$) and stellar masses (M_*) were fixed to values from the literature (see Table 1). The parameters z, γ, $T_{1\,\rm au}$, q, $r_{\rm char}$, and $M_{\rm H_2}$ were allowed to vary, and uncertainties on the best-fit models were estimated using MCMC resampling (Foreman-Mackey et al. 2013) with uniform priors spanning the grid space defined by Hoadley et al. (2015). The MCMC algorithm used 3000 walkers to explore the parameter space, finding no strong degeneracies between the six variables (see Figure 12 for an example corner plot). The final distributions of UV-H_2 flux were most sensitive to the values of $T_{1\,\rm au}$ and q used to define the radial temperature structure defined in Equation (5).

4.3. Radial Distributions of Flux from UV-H_2

Figure 11 shows the radial distributions of UV-H_2 flux that best reproduce the observed emission lines from the Lupus disks. The shapes of the gas distributions are generally correlated with the submillimeter dust distributions, in agreement with the results from Hoadley et al. (2015) that showed less UV-H_2 close to the star in disks with dust gaps or cavities. Sz 68, which is a close binary (Ghez et al. 1997), shows a distribution that is sharply truncated at 10 au. This is consistent with UV-H_2 emission from the primary component alone (Kurtovic et al. 2018), with Lyα photons reaching the gas surface layers out to the circumprimary disk edge. MY Lupi, which has two shallow gaps at 8 and 20 au (Huang et al. 2018), shows no sign of breaks in the gas disk at those radii, although the flux distribution declines rapidly from its peak at ~0.25 au. Finally, we report that the UV-H_2 emission in J1608-3070 extends to more distant radii than the other systems, with a flat distribution from ~0.3 to 10 au followed by a slow decline to the outer disk regions. This is consistent with the observed dust depletion inside of 75 au (van der Marel et al. 2018), which allows FUV photons to travel further in the disk and pump a more extended population of H_2 into vibrationally excited states. However, we note that the outer radius of the UV-H_2 distribution is limited by the *HST*-COS spectral resolution ($\Delta v \sim 17$ km s^{-1}). Given the stellar mass and disk inclination of J1608-3070, this corresponds to a spatial scale maximum of ~20 au.

Although the UV-H_2 lines do not originate from the same region as the submillimeter CN emission, the distributions of UV-H_2 flux provide constraints on either the radial extent of the population of H_2^* in surface layers of the gas disk or the location where those surface layers become optically thick to Lyα photons. However, the 2D radiative transfer models

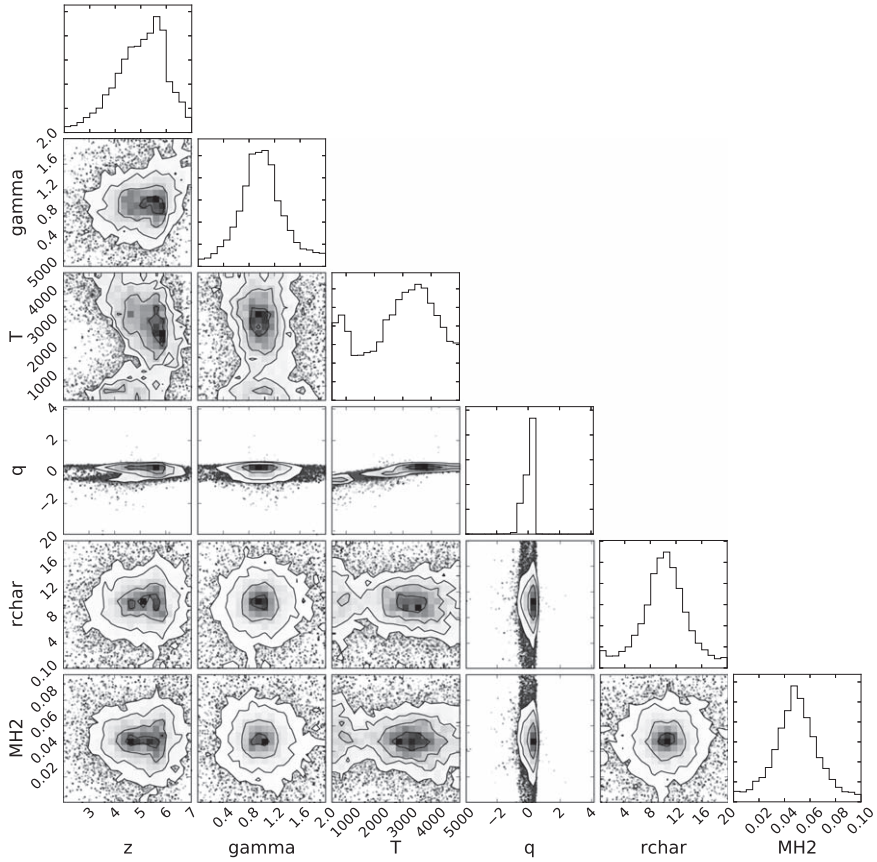

Figure 12. Corner plot showing marginalized probability distributions of the variable parameters, derived from MCMC resampling of the 2D radiative transfer models described in Section 4.1. This set of distributions was acquired by calculating log-likelihood values using the observed fluxes from the MY Lupi spectrum.

described above only include the thermal population of H_2^* and do not account for FUV-pumped gas located at more distant radii. Distinguishing between the Lyα-limited and H_2^*-limited scenarios for UV-H_2 emission, and subsequently identifying disk regions where H_2^*-driven CN formation pathways can proceed, will require a model that accounts for both the thermal and nonthermal gas populations. This relationship between the spatial distributions of H_2^* and CN will therefore be explored in more detail in a forthcoming paper.

5. Summary and Conclusions

We have analyzed the ultraviolet spectral properties of 19 young stars in the Lupus and Taurus-Auriga associations, using spectra from *HST*-COS and *HST*-STIS to directly measure fluxes from Lyα, the FUV continuum, semi-forbidden C II] λ2325, and UV-fluorescent H_2. Each of these is a potential tracer of the photochemical pathways responsible for producing CN and HCN molecules in disks. To investigate the formation chemistry of these two species, we compare the UV tracers to submillimeter CN and 14 μm HCN fluxes. We find that:

1. HCN fluxes are positively correlated with relative fluxes from the FUV continuum and C II] λ2325, implying that disks with strong continuum fluxes are more readily able to produce the atomic N and C^+ reactants required in the first step of the main HCN formation pathway.
2. By contrast, CN fluxes are negatively correlated with relative fluxes from the FUV continuum and C II] λ2325. This result indicates that, while molecule formation may proceed more efficiently when more atomic N is produced, CN destruction may increase accordingly as well.
3. Neither CN or HCN emission is significantly correlated with Lyα emission. However, we report very tentative positive (CN) and negative (HCN) correlations that are consistent with modeling work that predicts increased photodissociation with stronger Lyα irradiation.

We attribute the lack of correlations between CN and HCN emission and UV-H_2 fluxes to the spatial distributions of the three molecular species: the UV-H_2 is concentrated in surface layers of the inner disk, the submillimeter CN emission extends from the inner to the outer disk, and the HCN emission originates in deeper layers of the inner disk. By combining UV spectra with IR and submillimeter fluxes from UV-dependent molecular gas species, we are able to investigate model predictions of molecule formation pathways and observationally confirm that the FUV continuum plays an important role in regulating CN and HCN populations in protoplanetary disks. The analysis presented here can be extended to additional species (e.g., hydrocarbons) in the era of *James Webb Space Telescope*, which will enable higher spectral resolution observations of warm molecular gas and more accurate physical–chemical models of surface reactions in planet-forming systems.

We are thankful to the referee for thoughtful comments that helped strengthen the analysis presented here. N.A. is supported by NASA Earth and Space Science Fellowship grant 80NSSC17K0531 and *HST*-GO-14604 (PIs: C.F.

Manara, P.C. Schneider). H.M.G. was supported by program *HST*-GO-15204.001, which was provided by NASA through a grant from the Space Telescope Science Institute, which is operated by the Associations of Universities for Research in Astronomy, Incorporated, under NASA contract NAS5-26 555. We are grateful to M.K. McClure and C. Walsh for helpful discussions regarding the analysis presented here. This paper makes use of the following ALMA data: ADS/JAO. ALMA#2013.1.00220.S. ALMA is a partnership of ESO (representing its member states), NSF (USA) and NINS (Japan), together with NRC (Canada), MOST and ASIAA (Taiwan), and KASI (Republic of Korea), in cooperation with the Republic of Chile. The Joint ALMA Observatory is operated by ESO, AUI/NRAO, and NAOJ. This work utilized the RMACC Summit supercomputer, which is supported by the National Science Foundation (awards ACI-1532235 and ACI-1532236), the University of Colorado Boulder, and Colorado State University. The Summit supercomputer is a joint effort of the University of Colorado Boulder and Colorado State University. This research made use of Astropy,[10] a community-developed core Python package for Astronomy (Astropy Collaboration et al. 2013; The Astropy Collaboration et al. 2018).

Appendix
UV-H_2 Spectra and Modeling Results

We present the 2D radiative transfer models described in Section 4.2, which were fit to the nine strongest observed UV-H2 emission lines from each disk. The best-fit model emission lines and corresponding flux distribution are provided for MY Lupi (Figures 13–14), Sz 68 (Figures 15–16), and J1608-3070 (Figures 17–18). The remaining systems were previously fit by Hoadley et al. (2015). The corresponding model radial distributions of UV-H_2 flux for each system, with contours representing $\pm 1-\sigma$ bounds, are shown as well.

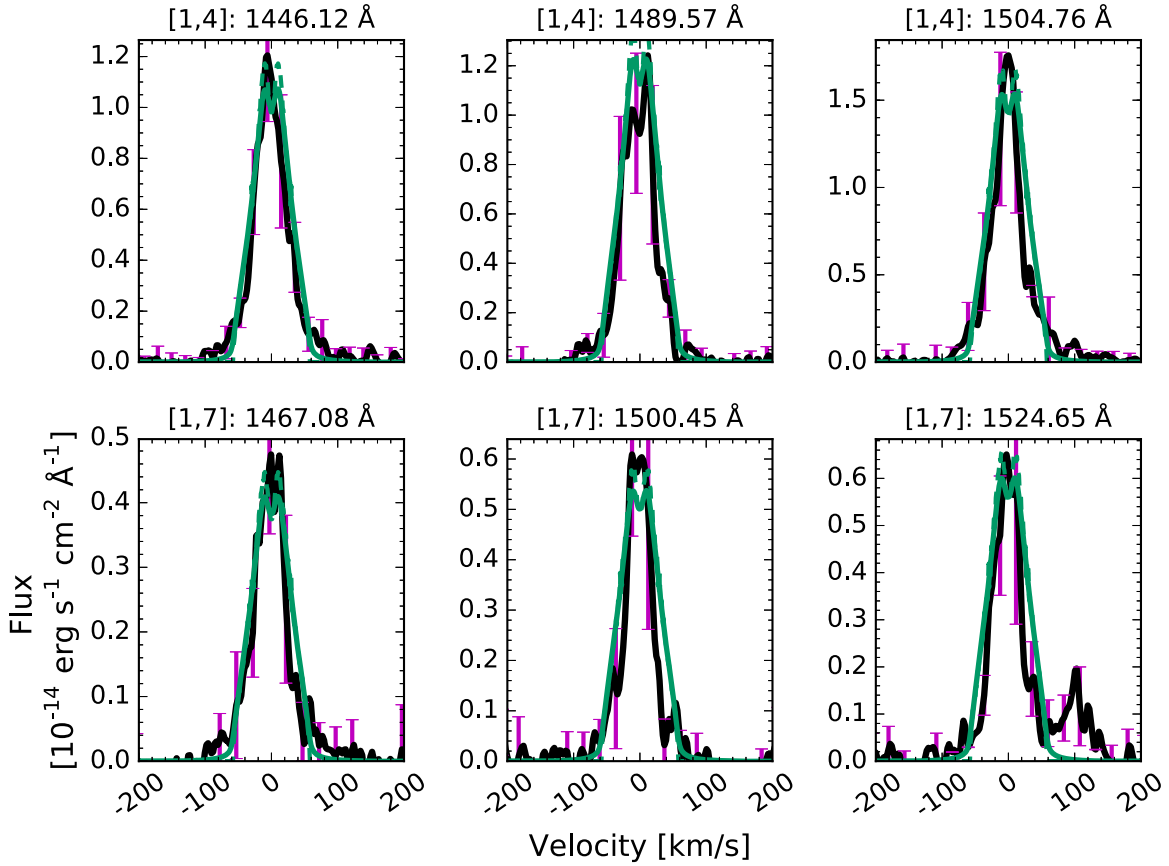

Figure 13. Observed UV-H_2 emission lines (black) and model distributions (teal) for MY Lupi. Dashed lines show the model profile prior to convolution with the *HST*-COS line spread function (LSF), while the solid lines are used to show the convolved line profile.

[10] http://www.astropy.org

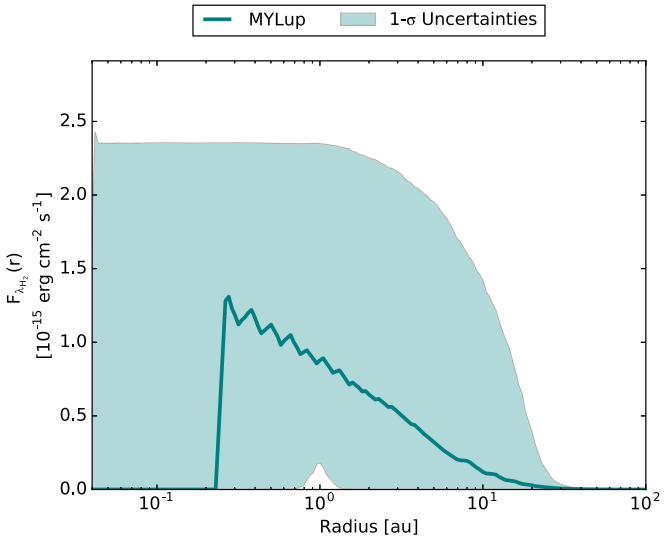

Figure 14. Best-fit model radial distribution of UV-H_2 flux from the disk around MY Lupi, with contours marking $\pm 1\sigma$ bounds on the median distribution. Uncertainties were estimated using MCMC sampling (Foreman-Mackey et al. 2013) over the parameter space defined by Hoadley et al. (2015).

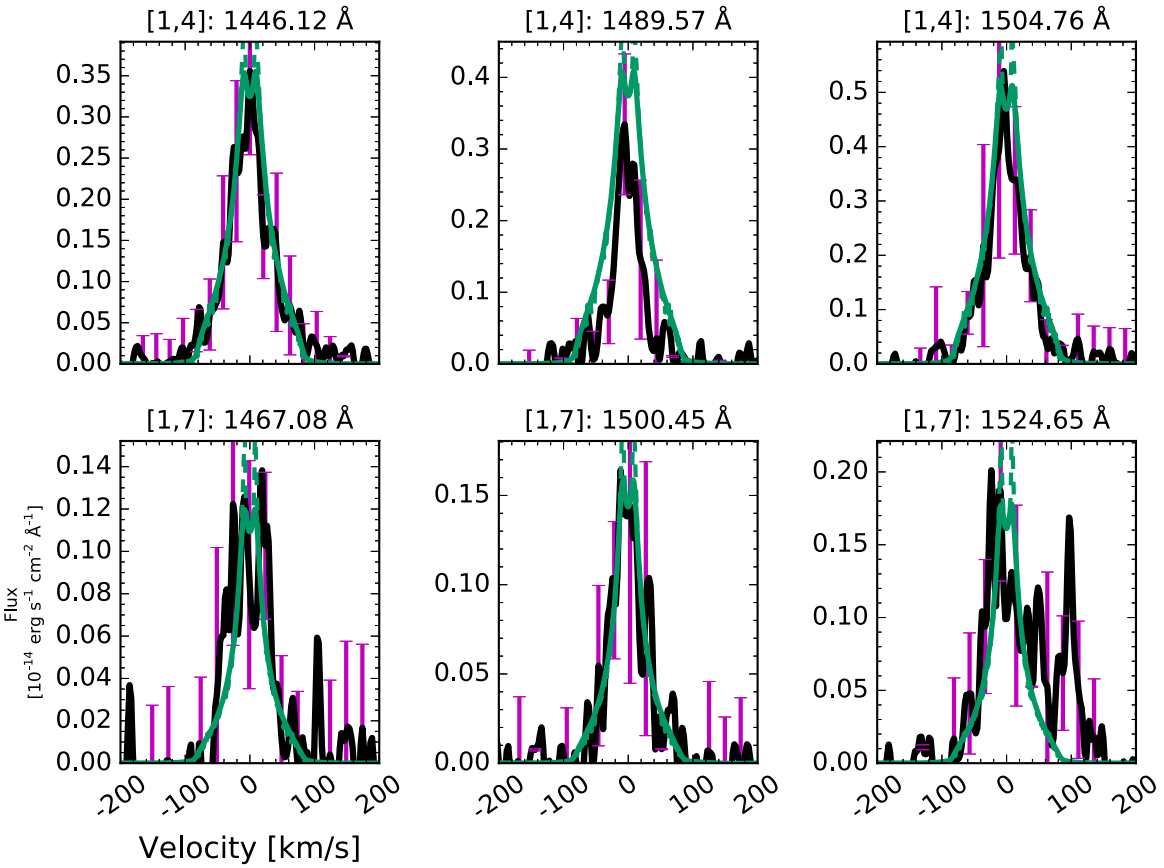

Figure 15. Observed UV-H_2 emission lines (black) and model distributions (teal) for Sz 68. Dashed lines show the model profile prior to convolution with the *HST*-COS line spread function (LSF), while the solid lines are used to show the convolved line profile.

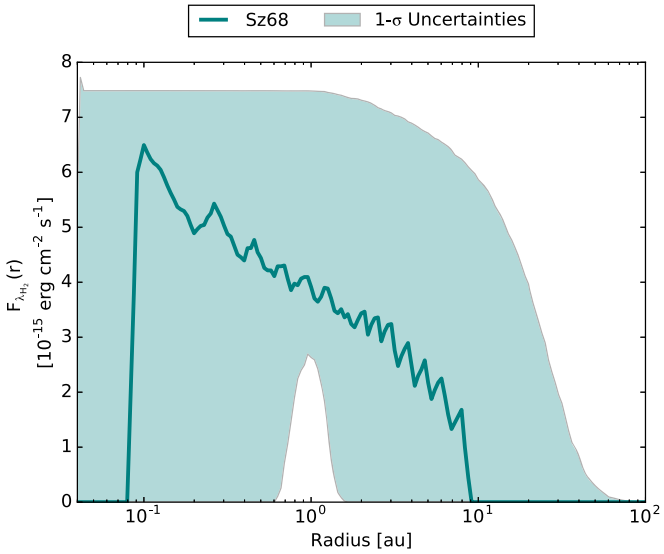

Figure 16. Best-fit model radial distribution of UV-H_2 flux from the disk around Sz 68, with contours marking $\pm 1\sigma$ bounds on the median distribution. Uncertainties were estimated using MCMC sampling (Foreman-Mackey et al. 2013) over the parameter space defined by Hoadley et al. (2015).

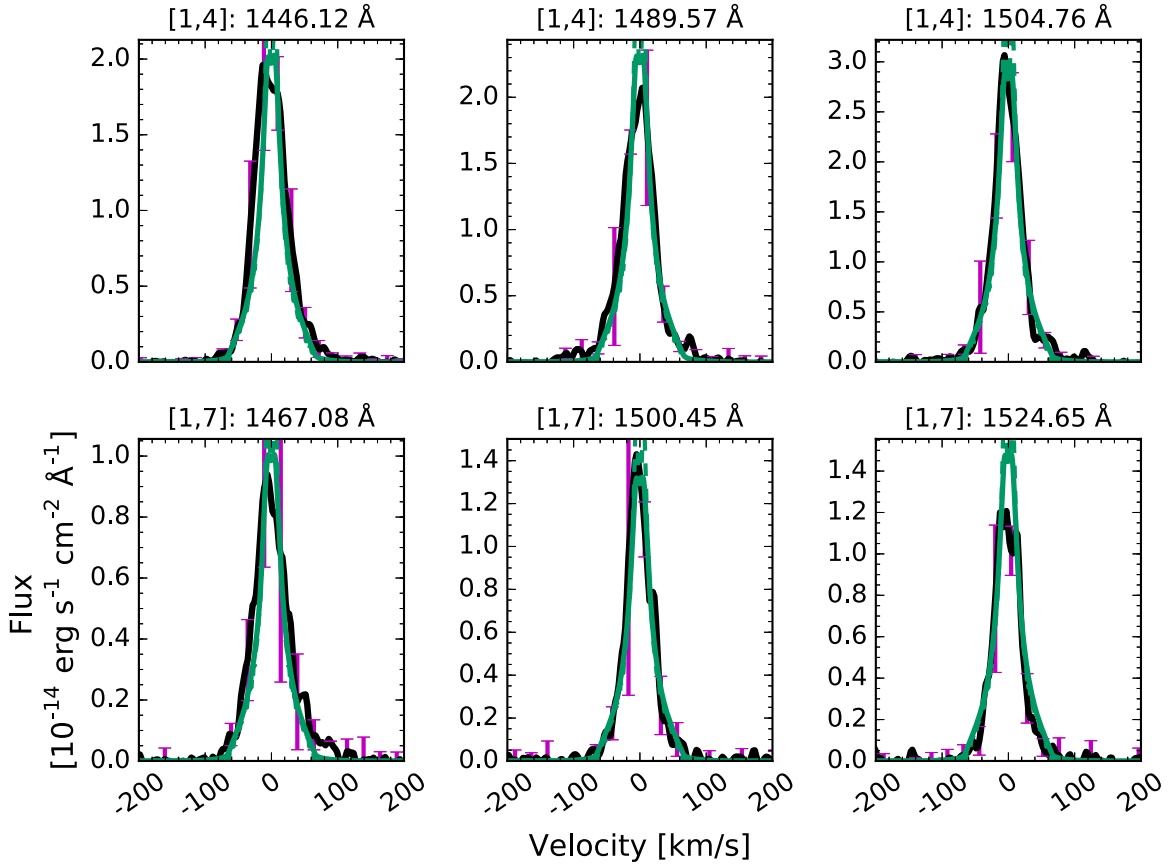

Figure 17. Observed UV-H_2 emission lines (black) and model distributions (teal) for J1608-3070. Dashed lines show the model profile prior to convolution with the *HST*-COS line spread function (LSF), while the solid lines are used to show the convolved line profile.

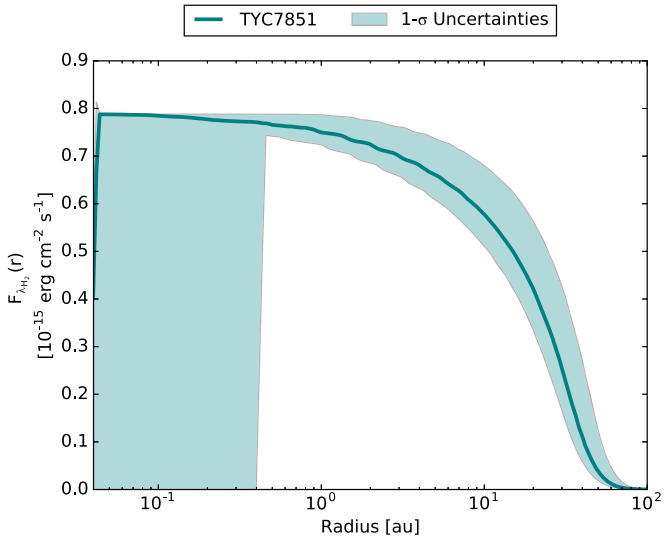

Figure 18. Best-fit model radial distribution of UV-H_2 flux from the disk around J1608-3070, with contours marking $\pm 1\sigma$ bounds on the median distribution. We note that the MCMC sampling (Foreman-Mackey et al. 2013) used to estimate the uncertainties on the flux distribution was carried out over a tighter parameter space than for the other two targets, since the signal-to-noise in the UV-H_2 emission lines is lower for J1608-3070.

ORCID iDs

Nicole Arulanantham https://orcid.org/0000-0003-2631-5265
Kevin France https://orcid.org/0000-0002-1002-3674
Carlo F. Manara https://orcid.org/0000-0003-3562-262X
Keri Hoadley https://orcid.org/0000-0002-8636-3309
Ewine F. van Dishoeck https://orcid.org/0000-0001-7591-1907

References

Ádámkovics, M., Najita, J. R., & Glassgold, A. E. 2016, ApJ, 817, 82
Agúndez, M., Cernicharo, J., & Goicoechea, J. R. 2008, A&A, 483, 831
Agúndez, M., Roueff, E., Le Petit, F., & Le Bourlot, J. 2018, A&A, 616, A19
Aikawa, Y., van Zadelhoff, G. J., van Dishoeck, E. F., & Herbst, E. 2002, A&A, 386, 622
Alcala, J. M., Manara, C. F., France, K., et al. 2019, A&A, 629, A108
Alcalá, J. M., Natta, A., Manara, C. F., et al. 2014, A&A, 561, A2
Alcalá, J. M., Manara, C. F., Natta, A., et al. 2017, A&A, 600, A20
Andrews, S. M., Rosenfeld, K. A., Kraus, A. L., & Wilner, D. J. 2013, ApJ, 771, 129
Andrews, S. M., Huang, J., Pérez, L. M., et al. 2018, ApJL, 869, L41
Ansdell, M., Williams, J. P., Manara, C. F., et al. 2017, AJ, 153, 240
Ansdell, M., Williams, J. P., van der Marel, N., et al. 2016, ApJ, 828, 46
Ansdell, M., Williams, J. P., Trapman, L., et al. 2018, ApJ, 859, 21
Ardila, D. R., Herczeg, G. J., Gregory, S. G., et al. 2013, ApJS, 207, 1
Arulanantham, N., France, K., Hoadley, K., et al. 2018, ApJ, 855, 98
Astropy Collaboration, Robitaille, T. P., Tollerud, E. J., et al. 2013, A&A, 558, A33
Bailer-Jones, C. A. L., Rybizki, J., Fouesneau, M., Mantelet, G., & Andrae, R. 2018, AJ, 156, 58
Banzatti, A., Pascucci, I., Edwards, S., et al. 2019, ApJ, 870, 76
Barenfeld, S. A., Carpenter, J. M., Ricci, L., & Isella, A. 2016, ApJ, 827, 142
Baulch, D. L., Cobos, C. J., Cox, R. A., et al. 1994, JPCRD, 23, 847
Bergin, E., Calvet, N., D'Alessio, P., & Herczeg, G. J. 2003, ApJL, 591, L159
Bergin, E., Calvet, N., Sitko, M. L., et al. 2004, ApJL, 614, L133
Bergner, J. B., Öberg, K. I., Bergin, E. A., et al. 2019, ApJ, 876, 25
Bethell, T. J., & Bergin, E. A. 2011, ApJ, 739, 78
Black, J. H., & van Dishoeck, E. F. 1987, ApJ, 322, 412
Bohlin, R. C., Savage, B. D., & Drake, J. F. 1978, ApJ, 224, 132
Bottinelli, S., Boogert, A. C. A., Bouwman, J., et al. 2010, ApJ, 718, 1100
Cazzoletti, P., van Dishoeck, E. F., Visser, R., Facchini, S., & Bruderer, S. 2018, A&A, 609, A93
Cazzoletti, P., Manara, C. F., Liu, H. B., et al. 2019, A&A, 626, A11
Chapillon, E., Guilloteau, S., Dutrey, A., Piétu, V., & Guélin, M. 2012, A&A, 537, A60
Cleeves, L. I., Öberg, K. I., Wilner, D. J., et al. 2016, ApJ, 832, 110
Cleeves, L. I., Öberg, K. I., Wilner, D. J., et al. 2018, ApJ, 865, 155
Dent, W. R. F., Thi, W. F., Kamp, I., et al. 2013, PASP, 125, 477
Espaillat, C. C., Robinson, C., Grant, S., & Reynolds, M. 2019, ApJ, 876, 121
Foreman-Mackey, D., Hogg, D. W., Lang, D., & Goodman, J. 2013, PASP, 125, 306
France, K., Roueff, E., & Abgrall, H. 2017, ApJ, 844, 169
France, K., Schindhelm, E., Bergin, E. A., Roueff, E., & Abgrall, H. 2014, ApJ, 784, 127
France, K., Yang, H., & Linsky, J. L. 2011a, ApJ, 729, 7
France, K., Schindhelm, E., Burgh, E. B., et al. 2011b, ApJ, 734, 31
France, K., Schindhelm, E., Herczeg, G. J., et al. 2012, ApJ, 756, 171
Ghez, A. M., McCarthy, D. W., Patience, J. L., & Beck, T. L. 1997, ApJ, 481, 378
Gómez de Castro, A. I., & Ferro-Fontán, C. 2005, MNRAS, 362, 569
Green, J. C., Froning, C. S., Osterman, S., et al. 2012, ApJ, 744, 60
Greenwood, A. J., Kamp, I., Waters, L. B. F. M., Woitke, P., & Thi, W.-F. 2019, A&A, 626, A6
Guilloteau, S., Di Folco, E., Dutrey, A., et al. 2013, A&A, 549, A92
Hartigan, P., & Kenyon, S. J. 2003, ApJ, 583, 334
Heays, A. N., Bosman, A. D., & van Dishoeck, E. F. 2017, A&A, 602, A105
Henning, T., Semenov, D., Guilloteau, S., et al. 2010, ApJ, 714, 1511
Herczeg, G. J., Linsky, J. L., Valenti, J. A., Johns-Krull, C. M., & Wood, B. E. 2002, ApJ, 572, 310
Herczeg, G. J., Wood, B. E., Linsky, J. L., Valenti, J. A., & Johns-Krull, C. M. 2004, ApJ, 607, 369
Herczeg, G. J., Walter, F. M., Linsky, J. L., et al. 2005, AJ, 129, 2777
Hoadley, K., France, K., Alexander, R. D., McJunkin, M., & Schneider, P. C. 2015, ApJ, 812, 41
Hoadley, K., France, K., Arulanantham, N., Loyd, R. O. P., & Kruczek, N. 2017, ApJ, 846, 6
Houck, J. R., Roellig, T. L., van Cleve, J., et al. 2004, ApJS, 154, 18
Huang, J., Andrews, S. M., Dullemond, C. P., et al. 2018, ApJL, 869, L42
Ingleby, L., Calvet, N., Herczeg, G., et al. 2013, ApJ, 767, 112
Johns-Krull, C. M., & Herczeg, G. J. 2007, ApJ, 655, 345
Kenyon, S. J., & Hartmann, L. 1995, ApJS, 101, 117
Kessler-Silacci, J., Augereau, J.-C., Dullemond, C. P., et al. 2006, ApJ, 639, 275
Kurtovic, N. T., Pérez, L. M., Benisty, M., et al. 2018, ApJL, 869, L44
Lebouteiller, V., Barry, D. J., Goes, C., et al. 2015, ApJS, 218, 21
Lebouteiller, V., Barry, D. J., Spoon, H. W. W., et al. 2011, ApJS, 196, 8
Li, X., Heays, A. N., Visser, R., et al. 2013, A&A, 555, A14
Long, F., Herczeg, G. J., Harsono, D., et al. 2019, ApJ, 882, 49
Long, F., Herczeg, G. J., Pascucci, I., et al. 2018, ApJ, 863, 61
Loomis, R. A., Öberg, K. I., Andrews, S. M., & MacGregor, M. A. 2017, ApJ, 840, 23
Loyd, R. O. P., France, K., Youngblood, A., et al. 2018, ApJ, 867, 71
Madhusudhan, N., Mousis, O., Johnson, T. V., & Lunine, J. I. 2011, ApJ, 743, 191
Manset, N., Bastien, P., Ménard, F., et al. 2009, A&A, 499, 137
McClure, M. K. 2019, A&A, 632, A32
McElroy, D., Walsh, C., Markwick, A. J., et al. 2013, A&A, 550, A36
McJunkin, M., France, K., Schneider, P. C., et al. 2014, ApJ, 780, 150
Miotello, A., van Dishoeck, E. F., Kama, M., & Bruderer, S. 2016, A&A, 594, A85
Miotello, A., van Dishoeck, E. F., Williams, J. P., et al. 2017, A&A, 599, A113
Miotello, A., Facchini, S., van Dishoeck, E. F., et al. 2019, A&A, 631, A69
Najita, J. R., Carr, J. S., Pontoppidan, K. M., et al. 2013, ApJ, 766, 134
Nuth, J. A., & Glicker, S. 1982, JQSRT, 28, 223
Öberg, K. I., Boogert, A. C. A., Pontoppidan, K. M., et al. 2008, ApJ, 678, 1032
Öberg, K. I., Qi, C., Fogel, J. K. J., et al. 2010, ApJ, 720, 480
Öberg, K. I., Qi, C., Fogel, J. K. J., et al. 2011, ApJ, 734, 98
Pascucci, I., Apai, D., Luhman, K., et al. 2009, ApJ, 696, 143
Pascucci, I., Herczeg, G., Carr, J. S., & Bruderer, S. 2013, ApJ, 779, 178
Pascucci, I., Testi, L., Herczeg, G. J., et al. 2016, ApJ, 831, 125
Pontoppidan, K. M., Salyk, C., Banzatti, A., et al. 2019, ApJ, 874, 92
Pontoppidan, K. M., Salyk, C., Blake, G. A., et al. 2010, ApJ, 720, 887
Salyk, C., Blake, G. A., Boogert, A. C. A., & Brown, J. M. 2011a, ApJ, 743, 112
Salyk, C., Pontoppidan, K. M., Blake, G. A., Najita, J. R., & Carr, J. S. 2011b, ApJ, 731, 130

Schindhelm, E., France, K., Burgh, E. B., et al. 2012a, ApJ, 746, 97
Schindhelm, E., France, K., Herczeg, G. J., et al. 2012b, ApJL, 756, L23
Schneider, P. C., France, K., Günther, H. M., et al. 2015, A&A, 584, A51
Schwarz, K. R., Bergin, E. A., Cleeves, L. I., et al. 2018, ApJ, 856, 85
Simon, M. N., Pascucci, I., Edwards, S., et al. 2016, ApJ, 831, 169
Skrutskie, M. F., Dutkevitch, D., Strom, S. E., et al. 1990, AJ, 99, 1187
Strom, K. M., Strom, S. E., Edwards, S., Cabrit, S., & Skrutskie, M. F. 1989, AJ, 97, 1451
Tazzari, M., Testi, L., Natta, A., et al. 2017, A&A, 606, A88
Teske, J. K., Najita, J. R., Carr, J. S., et al. 2011, ApJ, 734, 27
The Astropy Collaboration, Price-Whelan, A. M., Sipőcz, B. M., et al. 2018, astropy v3.0.5: a core python package for astronomy, Zenodo, doi:10.5281/zenodo.2556700
van der Marel, N., Williams, J. P., Ansdell, M., et al. 2018, ApJ, 854, 177
van Dishoeck, E. F., Jonkheid, B., & van Hemert, M. C. 2006, FaDi, 133, 231
van Terwisga, S. E., van Dishoeck, E. F., Cazzoletti, P., et al. 2019, A&A, 623, A150
van Zadelhoff, G. J., Aikawa, Y., Hogerheijde, M. R., & van Dishoeck, E. F. 2003, in SFChem 2002: Chemistry as a Diagnostic of Star Formation, ed. C. L. Curry & M. Fich (Ottawa: NRC Press), 440
Visser, R., Bruderer, S., Cazzoletti, P., et al. 2018, A&A, 615, A75
Walsh, C., Nomura, H., Millar, T. J., & Aikawa, Y. 2012, ApJ, 747, 114
Walsh, C., Nomura, H., & van Dishoeck, E. 2015, A&A, 582, A88
Williams, J. P., Cieza, L., Hales, A., et al. 2019, ApJL, 875, L9
Woodgate, B., Kimble, R., Bowers, C., et al. 1997a, BAAS, 29, 836
Woodgate, B. E., Kimble, R. A., Bowers, C. W., et al. 1997b, Proc. SPIE, 3118, 2
Yang, H., Herczeg, G. J., Linsky, J. L., et al. 2012, ApJ, 744, 121